ETH_zürich_

PAUL SCHERRER INSTITUT

Why the Dark-Field Signal of Porcine Lungs can be too Bright

An Investigation of the Small-Angle-Scattering Behavior of Porcine Lungs Depending on the Auto-Correlation Length

---

Master Thesis

Dominik B. Etter

Referee
Prof. Marco Stampanoni

Supervision
Dr. Michał Rawlik

X-Ray Tomography Group
Paul Scherrer Institute PSI
Department of Information Technology and Electrical Engineering
Swiss Federal Institute of Technology Zurich ETHZ

Zurich, 13$^{\text{th}}$ of September 2021

Abstract: Respiratory diseases constitute five out of the thirty most common causes of death and are responsible for 15 % of all deaths in Europe. To improve onset diagnostic of respiratory pathologies, dark-field imaging of the lungs is pursued at PSI where multiple grating-interferometry-based-projectional-radiography systems are operated. The means to handle, inflate and image excised lungs were established. Porcine lungs and PMMA spheres were imaged at auto-correlation lengths from 0.8 µm to 5.2 µm. Dominant feature size in healthy porcine lungs was found to be slightly bigger than 200 µm and the behavior of the dark-field signal and the thickness corrected R values were reported. The strong similarities between lung and PMMA spheres validates them as phantom material capable of simulating healthy as well as potentially pathological lung tissue. An upper limit for the auto-correlation length, capable to image human lungs at, was determined to be 0.73 µm and the influence of dose was demonstrated. These results provide the basis for a targeted design of a (pre-)clinical imaging system optimal to handle human lungs.

Contents

Introduction

The discovery of X-Rays is generally attributed to Prof. Wilhelm Röntgen who was the first to describe the observation of X-Rays in his initial report: *"On a new kind of ray: A preliminary communication"* in December of 1895. Although, this constitutes the first publication regarding X-Rays there have been a number of experiments and observed effects which retrospectively can be attributed to X-Rays. For example the observed darkening of sealed photographic tubes by Ivan Puluj in 1889 can best be explained by exposure to X-Rays. The earliest experiment, however, which unknowingly must have lead to the emission of X-Rays was performed more than 100 years before Röntgen's publication by William Morgan who passed electrical current through a partially evacuated glass tube and noted a glow effect.

After Röntgen's discovery their use and possible medical applications were quickly realized by Röntgen himself and others. Even before he submitted the afore mentioned paper, Röntgen had taken the first medical X-Ray image of his wife's hand which is famously known today as Röntgen's *"Hand mit Ringen"*. During the following decades projectional X-Ray imaging spread quickly and was used for all kind of investigations - from fast assessment of battlefield injuries during the 1st World War by mobile radiology cars to images taken solely to assess the fitting of new shoes in stores. While adversary effects were noticed rather quickly (many stories of burns, hair loss and worse were reported) it took until 1913 for the first safety guidelines for medical workers to be published by the German Roentgen Society and first laws in the US concerning maximal dose per day were only introduced in the mid 1930s.

For several decades projectional radiography remained the dominating and only form of X-Ray based imaging. It took until the 1960s when Allan Cormack came up with the mathematical algorithms for computed tomography (CT) reconstruction and Sir Godfrey Hounsfield built the first commercial CT scanner. The first patient was scanned in 1971 and since then CT imaging has revolutionized the field of medical imaging. Since then, it was possible to image individual parts of the human body with 3D spatial resolution. Even though the abilities of these first scanners were still strongly limited, the advantage of true 3D resolution lead to a fast and widespread implementation of CT-scanners in the medical world. Over the last two decades several technical advancements have been made enabling not only faster imaging at higher resolution, while constantly reducing the applied dose to the patient but paving the way for new imaging modalities and features. Most relevant to mention are CT perfusion imaging for detection and quantification of cerebral strokes, coronary computed tomography angiography (CCTA) for non-invasive evaluation of low- to moderate-risk chest pain with high sensitivity and specificity[1], iterative reconstructions algorithms and dual-energy CT which allows for more distinct classification of tissue and contrast agent[2].

Today, in most Western countries, the number of annually performed CT-scans is on an all-time high with a tendency to rise[3] and constitutes one of the most important parts in a radiologist's tool box. Despite huge advancements in the field, projectional radiography was not replaced by CT imaging as of today. This can mainly be attributed to three factors: Foremost, the cost of a CT scan is higher than for a single radiography, specifically due to higher initial costs and the required additional training for the operators. Secondly, the radiation dose received by the patient is mostly larger for CT scans than for conventional X-Ray imaging even though with the advent of ultra low dose CT there is barely a difference left for certain investigations[4]. Thirdly, CT scanners are still not as widely available as classic X-Ray systems, especially in less developed countries, and their operation and evaluation is more complex.[5]

Obviously, X-Ray imaging is also used in context of respiratory pathologies and diagnostics. Respiratory diseases constitute 5 out of the 30 most common causes of death. Specifically, Chronic Obstructive Pulmonary Disease (COPD) on third, lower respiratory tract infection on fourth, bronchial and lung cancer on sixth, tuberculosis (TB) on twelfth and asthma on the twenty-eighth place[6] contribute more than 15 % of all deaths in Europe or 500'000 annually[7] and are commonly referred to as "The Big Five". Simultaneously more than 1 billion people suffer from acute or chronic respiratory conditions world wide. While measures to prevent respiratory diseases have proven quite effective and efforts to improve air quality could drastically improve the situation, early detection of respiratory diseases are key to reduce those number under the given situation. COPD alone affects over 200 million people in the world and its formation is strongly linked to smoking next to other factors like general air pollution. Inhalation of tobacco smoke for example causes destruction of lung tissue (emphysema), obstruction of small airways and mucus deposition. In general such changes in the lung tissue get detected only once they reached an extent able to cause relevant functional impairment. Earlier detection is difficult and mostly coincidental.

Due to its simplicity, high cost efficiency and wide availability spirometry is the primary tool for COPD diagnostics and also the basis for several pulmonary function tests (PFTs). However, early stages of COPD and emphysema formation are almost impossible to detect with PFTs. Although in comparison, Computed Tomography (CT) is much more sensitive to diagnose emphysema and allows to assess its severity to some extent, it still underperforms in case of early stages of disease formation and onset diagnostics. This mainly due to a lack of contrast inside the pulmonary tissues and structures.

With the demonstration of Grating Interferometry (GI) based phase contrast by Pfeiffer et al in 2006[8], and the subsequent development of GI based dark-field (DF) contrast[9], obtained with X-Ray tubes rather than with synchrotron radiation, paved the way for the development of clinical applications of either contrast modality and both have been demonstrated repeatedly in small animal studies. Over the last four years significant advancements towards establishing scattering based image contrast in humans for clinical

purposes have been made: In 2017 Pfeiffer et al. first demonstrated an interferometer capable of handling human-sized subjects on living pigs[10]. Two years later, in 2019, Pfeiffer et al. imaged a human body post-mortem on their system demonstrating the additional value of dark-field images in combination with established methods[11]. In 2021, the same group demonstrated an improvement in diagnostic performance for emphysema by using dark-field imaging as an adjunct to state of the art CT-imaging in a cohort of 77 patients[12]. At the time of writing this, an additional study has just been published by Pfeiffer et al. establishing quantitative as well qualitative standards for healthy human subjects based on a cohort of 40 healthy patients[13]. These works represent the key advancements of (pre-)clinical dark-field imaging and demonstrate the additional value dark-field imaging can provide for patients.

In this work, the means to handle, inflate and image fresh porcine lungs are established and lungs as well as reference samples are scanned. So far, only very few values for dark-field signal in lungs at distinct auto-correlation lengths have been reported[14,15] raising the question for optimal sensitivity. The resulting data provides detailed insights into the behavior of the dark-field signal of lungs over a wide range of auto-correlation lengths and lays the basis to estimate the auto-correlation length for a clinical scanner.

An Overview of the Respiratory System

Starting at the nose and reaching to the most distal alveolus, the respiratory system includes the nasal cavity, the posterior pharynx, the glottis and vocal cords, the trachea and the entirety of the tracheobronchial tree. The upper airways consisting of all the structures from the nose to the vocal chords, are responsible to guide, filter and 'condition' the inhaled air. Here, 'conditioning' refers to adjusting the temperature and humidity of the inhaled air such that it does not cause any harm to the lower airways. The lower airways, consisting of trachea, conducting airways and alveoli, are responsible for the guidance and distribution of the air into the distal gas-exchanging units (respiratory units) which are themselves divided into three major parts: the respiratory bronchioles, the alveolar ducts and the alveoli. The bronchial structures are defined as the above mentioned conducting airways (ca. 150 ml) and constitute an anatomical dead space where no gas exchange occurs. With the respiratory bronchioles, the area of gas exchange starts and continues for only about 5 mm until the terminal alveoli are reached. These terminal 5 mm nevertheless constitute the major part of the lung volume of approximately 2.5 L and with a surface area of 70 m^2 at resting state. With an approximate diameter of 250 µm and polygonal shape, the alveoli contribute the major part of the lungs volume while being separated by alveolar septae. An average adult typically has about 5×10^8 alveoli with a density[2] of about 21.2 alveoli per mm^3. In humans, small pores (of Kohn) in the matrix of the alveolar septae connect adjacent alveoli to each

other and lead to collateral ventilation assisting in the prevention of alveolar collapse by allowing air flow between alveoli and separate respiratory ducts.

On a macroscopic level, the human lung is divided into the right and and left lung consisting of three (upper, middle, and lower) and two (lower and upper) lobes, respectively. The right lung is larger than the left one as the left hemithorax also contains the heart. In case of porcine lungs the left side strongly resembles the human left lung consisting of two lobes as well (cranial and caudal). The porcine right lung, however, contrasts the human right lung as it is divided into 4 lobes (cranial, middle, accessory and caudal). A further distinct difference from porcine lungs to human ones is found in the absence of collateral ventilation as barely any pores between adjacent structures can be found[16,17].

Both sides are covered by the two pleural membranes allowing for smooth gliding of the lung during expansion and contraction. If air enters this inter-membranous space, the resulting condition is referred to as pneumothorax. In case of liquid it is called a pleural effusion.

The primary function of the lungs is gas exchange in and out of the blood stream. Specifically, the transport and resupply of the blood with oxygen (O_2) and the removal of carbon dioxide (CO_2) from the blood. The lung can accommodate large volumes of blood at low pressure and features a unique duality in its blood supply. The pulmonary circulation refers to the blood passing through the lung to resupply itself with O_2. The blood supply, providing the lung tissue itself with O_2, is organized independently and referred to as the bronchial circulation. The pulmonary circulation starts in the right ventricle of heart where deoxygenated blood is pumped into the pulmonary artery which quickly divides leading to the left and right lung. Interestingly, the only arteries carrying deoxygenated blood are the ones of the pulmonary circulation. The arteries progressing into the lungs, divide further and become increasingly smaller forming the largest capillary bed in the human body. The pulmonary circulation contains approximately 500 mL of blood or roughly 10 % of the blood volume in an adult. The capillary bed contains ca. 75 mL of blood at any time. This volume can increase to up to 200 ml during exercise due to increased pressure and flow. A unique feature of the lungs is the subsequent recruitment of new capillaries to compensate in the situation of stress - such as exercise - to further increase its capacity. The capillary bed covers a surface similar to the alveoli of about 70 - 80 m^2. The separation between the erythrocytes and the air space is only about 1 µm to 2 µm which is ideally suited for passive diffusion of O_2 and CO_2 in and out of the blood stream. After passing through the capillary bed the freshly oxygenated blood is collected into larger pulmonary veins which finally return the oxygenated blood into the left atrium of the heart via the pulmonary vein[18].

The main goal of breathing is to move the air in and out of the lungs to enable repeated gas exchange in the lungs. Under healthy conditions the chest wall and the lungs move

together and display equal changes in their respective volumes. At the end of inspiration and exhalation there is no pressure gradient between the alveolar space and the surrounding atmosphere, accordingly no airflow occurs. During inspiration the muscles of the diaphragm and the chest wall contract leading to a downward movement of the diaphragm and an out- / up- ward movement of the chest wall. Consequently a decrease in alveolar pressure results causing inward air flow assuming the glottis is opened. During exhalation the muscles relax and the diaphragm moves upwards in the chest leading to positive alveolar pressure, the glottis opens and outward air flow progresses until the pressures equalized again. During relaxed inspiration respiratory pressures in the order of -1 cm H_2O or $\sim -10^{-3}$ bar[18] are reached in relation to the surrounding atmospheric pressure. In case of exercise or forced inspiration pressures of up to -100 cm H_2O or $\sim -10^{-1}$ bar can be reached[19].

During normal breathing about 500 ml of air are moved in and out of the lungs, the so-called tidal volume V_T. The total lung capacity (TLC) in a healthy individual is approximately 6 L which can be reached with forced maximal inspiration. If followed by maximal exhalation the difference between the TLC and residual volume (RV) in the lungs is referred to as the forced vital capacity (FVC). The RV is defined as minimal volume of air, contained in the lungs after forced maximal exhalation. The easiest and most popular way to assess lung volumes is via spirometry (see Fig.1). Spirometry is conducted with the help of spirometer which measures the volumetric in- and out- put during relaxed breathing an forced inhalation via a mouth piece[18].

It is important to note that the lung is a highly dynamic system which displays elastic properties that are essential to its function, pressure regulation and maintenance. Lung compliance (C_L) is a measure of the lungs elasticity and defined as the change in volume V resulting from a 1 cm H_2O change ($\sim -10^{-3}$ bar) in the distending pressure P. High lung compliance represents easy extension of the lung while a low compliance represents a 'stiff' lung. Normally expressed as $C_L = \Delta V/\Delta P$ the compliance of a healthy human lung is approximately 0.2 l/cm H_2O, although it varies significantly depending on the current state of inflation. Lung compliance is strongly linked to the presence of lung surfactant which is part of the liquid-air interface and secreted by specialized cells in the lung tissue. The surfactant which mainly consists of lipids has several important roles in lung physiology. It decreases the surface tension in the liquid-air interface leading to a reduced workload due to reduced tension forces, prevents collapse and sticking of alveoli during exhalation and generally stabilizes alveolar structures. To maintain the lipid monolayer provided by the surfactant at the alveolar-air interface, regular dilation and contraction of the lung tissue exceeding the values during tidal breathing are necessary. Such elastic movements are achieved by regular yawning and sighing leading to larger changes in the lung volume than under relaxed conditions[18]
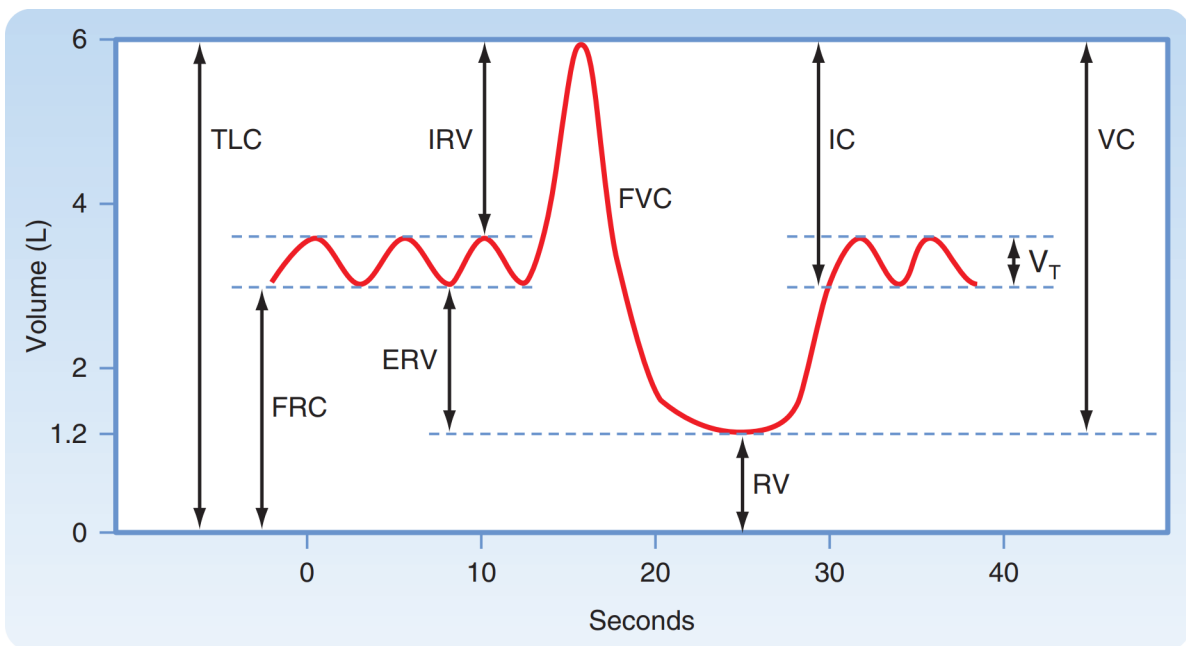
Fig. 1: Various lung volumes during a pulmonary function test (PTF) via Spirometry. ERV,expiratory reserve volume; FRC, functional residual capacity; FVC, forced vital capacity; IC, inspiratory capacity; IRV, inspiratory reserve volume; RV, residual volume; TLC, total lung capacity; VC, vital capacity; VT, tidal volume. (Adapted and modified from [18])

Established Methods for Lung Imaging

In light of recent focus and development on bedside modalities such as thoracic ultrasonography and electric impedance tomography the recognition of computed tomography as the "gold standard" might appear out-dated. However, CT should be considered the gold standard by which emerging modalities are compared which is elaborated in the following[20].

Lung CT is used in the diagnosis and classification of COPD, emphysema, fibrosis, lung cancer and further respiratory pathologies. It allows to visualize airways as small as 1 mm and to display bronchial wall thickening, mucus plugging, and parenchymal infiltrates[21]. With the ability to quantify average tissue density (quantitative CT, qCT) via the reconstructed density values in individual volumes of interest (VOI) it is possible to classify hyper-, normal-, poor- and non-aerated segments. This is specifically relevant in cases of acute respiratory distress syndrome (ARDS), acute lung injury (ALI) and verification of proper mechanical ventilation[22]. Despite the advancements in technology, CT based lung imaging poses certain pit falls. The soft tissues present in the lung only differ slightly with respect to their attenuation coefficients which in turn makes it difficult to differentiate them accurately on conventional chest CT investigations and complicates accurate detection of lung disease. Additionally, it has repeatedly been shown that different scanning and reconstructions parameters significantly influence the quantitative analysis of lung scans especially in context of hyper-aerated lungs and emphysema[23,24]. Unification of CT protocols and parameters has been recommended but seems impossible regarding multiple manufacturers, a plethora of different models, financial limitations and the constant advancement of algorithms and hardware. Last but not least, the associated radiation exposure, the required mobilisation of the patient and the associated discomfort as well as possible harm are valid concerns regarding all X-Ray based imaging methods and have to be addressed by the physician in charge. Recent investigations into bedside modalities for lung imaging (lung ultra sound and electrical impedance tomography) show promising results and start to get close to the performance of CT in terms of diagnostic and clinical power under certain conditions - mainly in context of critical care.

Thoracic ultrasonography or more commonly referred to as lung ultra sound (LUS) developed into an invaluable tool in critical care units as it allow to investigate the lung and pleural space at the bedside and without any radiation exposure. Over the last decade, several consensus papers have been published regarding the LUS semiology and its applications[25–28]. Furthermore, it has been shown that LUS is highly effective in assessing a number of pulmonary pathologies such as pneumothorax, pleural effusion, acute dyspnea, pulmonary edema versus ARDS, pulmonary embolism and pneumonia as well as in the guidance and assessment of mechanically ventilated patients[29]. In light of the COVID-19 pandemic, more attention was brought to LUS. The national

library of medicine more commonly known as PubMed.gov featured 5094 publication containing the words "ultrasound" and "COVID-19" between 2020 and 2021 while only 3809 publications were found for the words "computed tomography" and "COVID-19" during the same period[30,31], highlighting its relevance. It has been shown that LUS performs with a sensitivity distinctly above 90% and acts as an strong independant predictor for RT-PCR based COVID-19 tests[32]. This not only rivals the performance of CT[33,34] but also allows for improved patient management and workflow optimization, such that the limited imaging resources can be used in a most efficient way while the mentioned advantages of LUS compared to CT still hold. Finally, the ease of sterilization of the ultrasound probe compared to a CT scanner and the reduced risk of transmittance due to bedside imaging underline these advantages. It is strongly recommended to employ LUS for patient assessment, triage and monitoring of disease progression[35].

In contrast to LUS, electrical impedance tomography (EIT) is in its infancy and only a few commercialised, clinically approved EIT systems for ICU monitoring are available at this point. It is based on measurements of surface electrodes from which electrical impedance, conductivity and permittivity are inferred and a tomographic image of the body part of interest can be reconstructed. Similar to LUS it can be performed at the bedside and no radiation exposure occurs as alternating currents are applied to the electrodes and the equi-potentials measured from all electrodes allow for image formation. The image reconstruction requires to find a solution to a severely ill-posed, non-linear inverse problem which was first formulated by Alberto Calderon in 1980[36]. As no two bodies are the same and user-errors in electrode placement are unavoidable a standard shape is assumed for reconstruction which often introduces artifacts and errors into the final images. Besides EIT, currently no image modality suitable for continuous non-invasive bedside monitoring of infant lung function exists. While this might sound like an oddly specific applications the fact that 15 millions babies are prematurely born each year many of which suffer from respiratory failure underlines the importance of EIT and its further development[37]. EIT is specifically well suited for lung imaging as the lung tissue conductivity is about five times lower compared to most other soft tissue which results in a high absolute contrast. As lung resistivity in- and de-creases several-fold during a breathing cycle, ventilation monitoring is a promising clinical application of EIT since mechanical ventilation can regularly lead to ventilator-associated lung injury (VALI)[38]. Current key problems with EIT is the slow rate of transition of new algorithms and hardware into clinical useful tools as well the lack of maintaining imaging standards (e.g. DICOM) for image reconstruction algorithms. A detailed introduction to EIT and reconstruction algorithms can be found here [39].
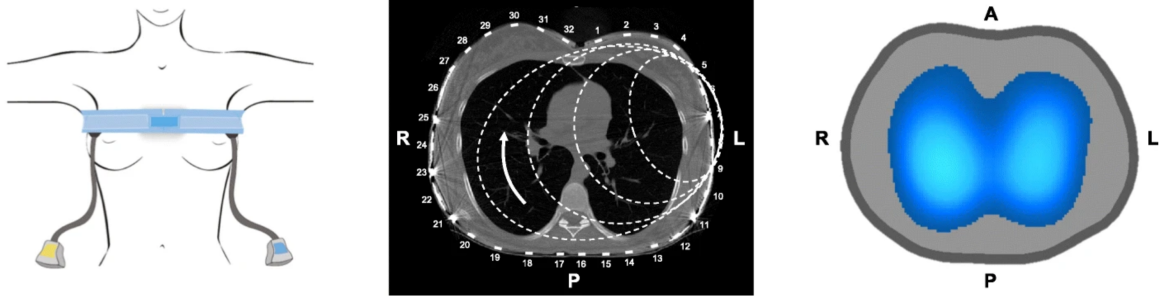
Fig. 2: *Left:* Placement of electrode belt on chest. *Middle:* Computed tomographic axial slice of thorax with 32-electrode belt, and schematic representation of electrical current pathways through thorax. One pair of electrodes injects electrical current while remaining electrodes read voltages produced as a result of the distribution of current density inside thorax. Injection pair is alternated sequentially, and after a full cycle one image will be generated. *Right:* Functional image reconstructed by electrical impedance tomography (EIT) using a color scale: the lighter the blue, the greater the regional ventilation. A, anterior; L, left; P, posterior, R, right. (Adapted and modified from [40])

The Basis of X-Ray Imaging

Conventional X-Ray imaging is based on the Lambert-Beer law which describes the reduction in the photon flux per unit length. Equating the change of photons dN to the number of photons at a given depth dx yields

$$dN = -\mu N dx, \tag{1}$$

where μ is the linear attenuation coefficient (LAC). Solving this differential equation by integration gives the Lambert-Beer law.

$$N = N_0 e^{-\mu x}. \tag{2}$$

The LAC describes how much radiation is absorbed per distance in a given material and at a certain energy. Since the exponent must be dimensionless the dimension of μ result to per length. The amount of photon flux traversing the sample of interest is measured by a X-Ray detector behind the sample, which in combination with a flat field scan, allows for calculation of the exponential term $-\mu x$ containing the LAC μ and the traversed sample thickness x. Dark regions represent higher levels of absorption while bright regions represent low levels of absorption. Keep in mind that in hospital mostly the negative representation is used, such that bones appear white (strong absorption) and soft tissue appears dark (weak absorption). Absorption-based contrast formation

as described here works well for material with 'large' differences in their LAC but for differentiation of soft tissues (e.g. within breasts) the contrast is very low as different soft tissues have very similar LACs (see Table 1).

Type	Tissue	LAC / [cm^{-1}]
Soft Tissue	Lung Tissue	0.177975
	Adipose Tissue	0.160360
	Breast	0.172176
	Soft Tissue	0.179458
Hard Tissue	Bone, Cortical	0.356160

Table 1: Examples of linear attenuation coefficients for different types of tissue at $100\,\text{keV}$[41]. While all types of soft tissue have values in the range of $0.16 - 0.18\,\text{cm}^{-1}$, bone has almost twice that, highlighting the difficulties of soft tissue contrast based on X-Rays.

Attenuation coefficients are, however, clearly dependent on the energy of the X-Ray beam. This allows for a maximization of contrast by using low energy X-Rays as the differences in LACs is larger. In the case of mammography, the use of low energy X-Rays additionally allows to distinguish micro-calcifications. In light of their potential malignancy and association to breast cancer formation this constitutes an additional advantage in using low energy X-Rays[42].

Beyond Absorption

While image formation based on attenuation is certainly the oldest and most dominant technique employed, there are other options for contrast formation. While X-Ray differential phase contrast (DPC) imaging is based on refractive properties of the sample, dark-field (DF) imaging makes use of small angle scattering which occurs at interfaces between materials with different electron densities, e.g air-tissue interfaces in the lung. Phase and dark-field contrast have been used in the regime of visible light for quite some time but proved hard to transfer and implement in the regime of X-Rays[9]. However, in the early 2000s distinctive advancements have been made. It has been demonstrated that all three signals (absorption, DPC and DF) can be quantitatively assessed by means of grating interferometry (GI)[8,9] which will be explained in more detail in section *Talbot-Lau Grating Interferometry*. First though, an explanation of underlying physical principals of phase and dark-field imaging follows.

Phase Contrast and Snell's Law

Even though X-Rays have much higher energies than visible light the same optical principles do still apply. The laws of refraction are just as valid in the X-Ray regime as they are in the optical regime although deflection angles are much smaller and refractive indices are negative for most materials. The information represented by the DPC is based on the detected deflections of the X-Rays by the sample rather than by absorption. Deflection occurs due to small variations in local electron density of the sample, which results in a higher contrast for soft tissues or low-Z materials if compared to absorption. Refractive behavior of light is described by Snell's law. Light takes the fastest path between two points in a given medium resulting in a straight line. If the two points lie in different media, the path taken has to be optimized by taking into account the different speeds of light (represented by the refraction index). This forms the basis of Snell's Law:

$$n_1 \sin(\varphi_1) = n_2 \sin(\varphi_2). \tag{3}$$

The index of refraction (here n_i) is complex valued

$$n_{complex} = 1 - \delta + i\beta\,, \tag{4}$$

where β represents the attenuation and δ the phase shift. If inserted into a complex wave function we receive two terms:

$$\Psi(x) = \Psi_0 e^{i(1-\delta)kx} e^{\beta kx}\,, \tag{5}$$

which represent the phase shift and the attenuation therefore allowing for direct comparison of the two effects. In case of X-Rays, the refractive index $n_{complex}$ is relatively close to 1. Looking at a transition of a low energy X-Ray at $20\,\mathrm{keV}$ from vacuum into water one finds $\beta = 3.99411 \times 10^{-10}$ and $\delta = 5.76149 \times 10^{-7}$. Moving to higher energies, this difference will further increase but already at 20 keV the refraction effect should be roughly 1000 times stronger[43].

While in theory this looks like a massive advantage of DPC over absorption imaging, in practice the resulting advantage is often much smaller. While absorption imaging requires the means to detect and quantify the amount of X-Rays passing through a sample, DPC requires a more intricate setup. Either a coherent X-Ray source is required (e.g. a synchrotron) or grating interferometry (GI) needs to be employed to access the required phase information. GI is based on optical interferometry which is phase sensitive, however, it requires optical gratings with small pitches to provide enough sensitivity to small scattering angles and deep enough structures for enough interaction. Such gratings are still challenging and rather expensive to produce which limits today's DPC imaging approaches - especially at higher energies. Still, these are not physical
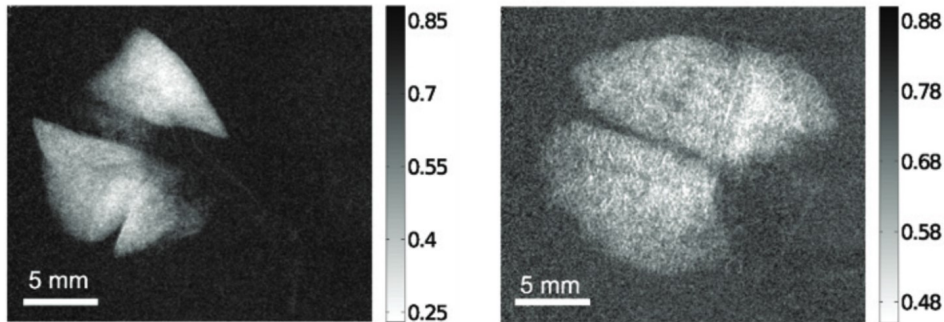
Fig. 3: *Left:* Dark-field image of healthy murine lungs *ex vivo*. *Right:* Dark-field image of emphysematous murine lungs *ex vivo*. Note the patchiness of the emphysematous lungs and the reduced dark-field signal in large parts (Adapted and modified from [44]).

limitations as in the case of absorption based imaging and therefore future developments beyond the abilities of absorption imaging are possible.

Small Angle Scattering and the Dark-Field Signal

Small angle scattering occurs when photons pass through multiple material interfaces of different electron densities, causing a small deflection on each transition. These refraction angles are to small to be resolved directly by the imaging system. However, macroscopically, a blurring of the otherwise well defined interference pattern results which in turn can be quantified as a loss in visibility yielding the dark-field signal (see *Talbot-Lau Grating Interferometry* below). The dark-field signal represents the amount of small angle scattering / deflections that occurred while the beam traversed the sample and carries information about the samples microstructure which is not directly resolvable by the detector.

The degree of scattering is roughly proportional to the number of interfaces traversed by the beam. It is therefore apparent that the lung with its microstructure of alveolar septae and air spaces is expected to produce a strong scattering signal. This has practically been shown in a mouse model already back in 2013[45] and numerous further animal studies have since been published. The advantage of dark-field imaging lies in its sensitivity to changes in the microstructure of the sample which are not directly resolveable by the detector. As described above, detection of pathological changes in the lung tissue (e.g. emphysema) with conventional X-Ray or CT imaging is only possible once a certain degree of severity is reached and macroscopic changes become apparent. Early stages of disease formation remain hard to detect. Dark-field imaging allows to detect those early, microscopic changes in the lung as the scattering behaviour changes with the

dominant present feature size. In the case of emphysema, an increase in alveolar airspace is observed due to destruction of alveolar septae. Fewer septae will lead to less scattering and therefore a higher visibility (lower dark-field signal). Fig. 3 shows an example of a healthy and diseased murine lung with decreased dark-field signal representing the foci of disease formation.

Talbot-Lau Grating Interferometry
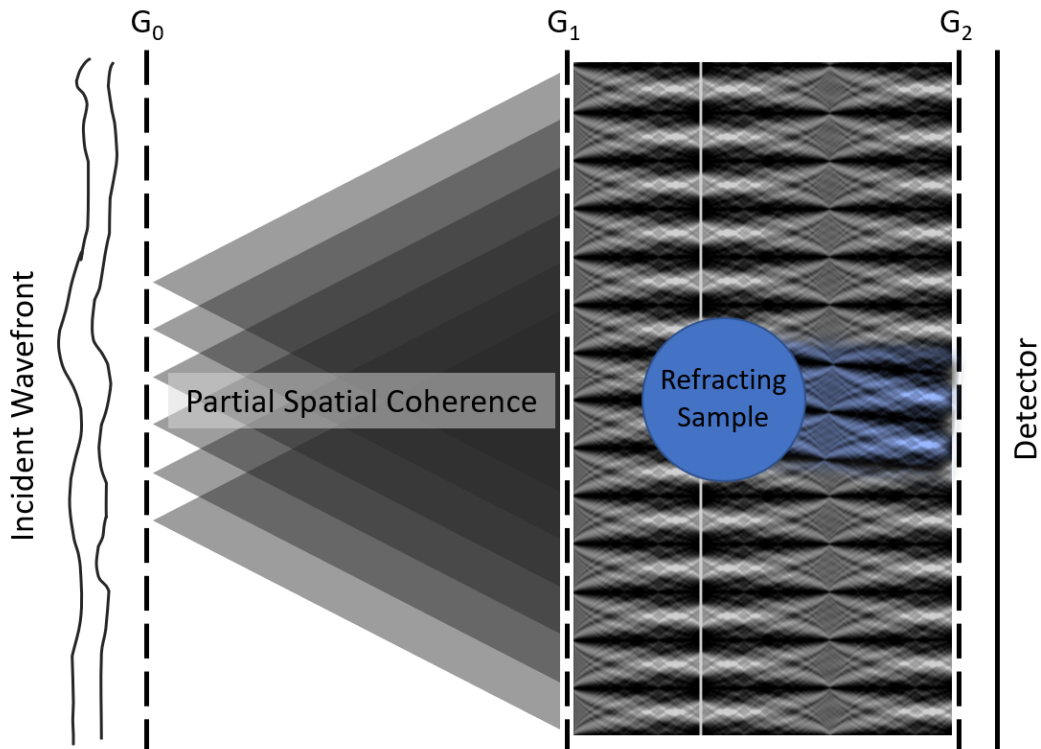
Fig. 4: Schematic representation of a Talbot-Lau grating interferometer. From left to right: The incident wave front hits G_0 and partial spatial coherence results. G_1 generates the Talbot carpet which is altered by the sample. G_2 is stepped and the signal is recorded. Note the shifted peaks of the blue part of the Talbot carpet compared to the grey parts.

To access the phase signal without the presence of a coherent source, a Talbot-Lau grating interferometer (TLGI) employs three optical gratings, two of which are absorption gratings while one is a phase grating. The first grating, called G_0, is an absorption grating leading to partial spatial coherence. G_1 is a phase grating, creating the Talbot carpet and G_2 is the second absorption grating used as an analyzer for the Talbot carpet as is shown in Fig. 4.

G_0 and G_2 have supporting roles while G_1 is most relevant for the function of the interferometer. X-Rays passing through the bars of the G_1 grating experience a relative phase shift of 0 to 2π allowing for interference. Due to the Talbot-Effect a repeating intensity pattern known as the Talbot carpet (see Fig. 4) results. G_2 is ideally placed at a distance to G_1 where minima and maxima of the intensity pattern are most easily distinguished. This is the case after each multiple of the so-called Talbot distance. As the pattern periodically repeats, there are theoretically an infinite amount of possible locations to place it.

As hinted above, G_0 and G_2 are mostly relevant to circumvent certain engineering problems. G_2 is used as an analyzer grating. As the intensity pattern is generally much smaller than an individual pixel of a detector and as such not directly resolvable, the use of such an analyzer grating is required. It allows to sample the intensity pattern indirectly by superimposing it with the grating. Crucially, G_2 must have the same period as the Talbot carpet at G_2's location along the beam axis.

G_2 is an absorption grating which only allows parts of the interference pattern to pass through its slits and hit the detector. By moving G_2 perpendicular to the beam axis and acquiring an image at each position the pattern is sampled which allows for subsequent signal reconstruction. A process which is also referred to as "phase stepping" and is further explained in the next section *Signal Retrieval and Parameters*.

So far, G_1 provides an interference pattern and G_2 allows to sample it even though detectors cannot resolve it directly. G_0 now addresses the last practical problem. For interference effects to be observed, a high degree of coherence is necessary. Medically relevant X-Ray sources/tubes generally provide a low-coherence beam. Introduction of the absorption grating G_0 (sometimes also called source grating) can be seen as a way of creating a large amount of very small slit sources, leading to a much higher degree of coherence, necessary for interference effects. Effectively, each individual grating slit will then create an interference pattern downstream. If geometries and grating properties are chosen adequately, all these periodic structures are aligned and add up at the detector allowing for proper imaging.

In case of phase contrast imaging the minimal resolveable refraction angle α_{min} characterizes an interferometer setup with respect to the obtainable contrast of small electron density variations. It is given by

$$\alpha_{min} = \frac{p_2}{d}\frac{\Delta\phi}{2\pi} \qquad (6)$$

where p_2 denotes the period of G_2, d the distance of the sample to G_2 and $\Delta\phi$ the phase shift. This is can be understood intuitively as a phase shift of $\Delta\phi = 2\pi$ results in a shift

of exactly p_2 on the detector and as α_{min} is very small, the small angle approximation of $\tan(\alpha) \approx \alpha$ holds.

In case of dark-field imaging, the setup is characterized by the auto-correlation length

$$\xi = \frac{\lambda L_s}{p_2} \tag{7}$$

where λ is the wavelength of the X-Rays and L_s is the distance of the sample to G_2. Note that this formula is valid while the sample is placed between phase and analyzer grating. If the auto-correlation length is varied it is possible to fully quantitatively characterize a sample for its scattering structures of different size and volume fraction. To some degree the auto-correlation length can be seen as measure to what structure size the system is most sensitive to. Therefore, a setup has to be tuned in such a way to return optimal contrast for the sample at hand. Tuning of the auto-correlation length can be achieved by varying one of the three variables in Eq. 7. While varying the wavelength/energy and grating period can be rather expensive in financial terms as well as in performance, changing the position of the sample is more feasible but brings with it another set of problems. The setup in Fig. 4 shows a parallel beam geometry. Often, however, a fan beam or conical setup is used. This means that if the sample is moved alongside the beam axis the geometric magnification changes as well and measurements taken at different auto-correlation lengths are no longer directly comparable (see *Inverse Geometry Setup*).

As a conventional Talbot-Lau GI employs two absorption gratings (G_0 and G_2) $\sim 75\,\%$ of all emitted photons and $\sim 50\,\%$ of all photons traversing the sample are lost (assuming a duty cycle of 0.5). This eventually leads to a much poorer dose efficiency, which is critical for medical applications - especially as gratings for high energies are hard to manufacture.

Signal Retrieval and Parameters

By stepping G_2 and recording an image at each position, an intensity curve for each pixel is measured. This is done with and without sample in the beam's path producing a flat-field/reference image and the sample image, referenced by the indices $i = f, s$, respectively. Fitting

$$I_i(x) = I_{0,i}(\mu)(0.5 \cdot V_i \cdot \cos(x + \varphi_i) + 0.5) \tag{8}$$

to the recorded intensity curves, where I_0 denotes the initial intensity, V_i the visibility, φ the phase offset and x the position of the phase step, returns the required parameters to

calculate all three images (see Fig. 5): Namely these are the attenuation Γ, the differential phase $\Delta\varphi$ and the dark-field Σ image:

$$\Gamma := -\ln\left(\frac{I_{0,\mathrm{s}}}{I_{0,\mathrm{f}}}\right), \quad \Delta\varphi := ((\varphi_{\mathrm{s}} - \varphi_{\mathrm{f}} + \pi)) \bmod 2\pi, \quad \Sigma := -\ln\left(\frac{V_{\mathrm{s}}}{V_{\mathrm{f}}}\right) \tag{9}$$

The dark-field signal therefore is defined as the logarithmic visibility reduction. It is impertinent to realize that an individual intensity curve as shown in Fig. 5 corresponds to one pixel of the detector forming the basis for distinct image formation.
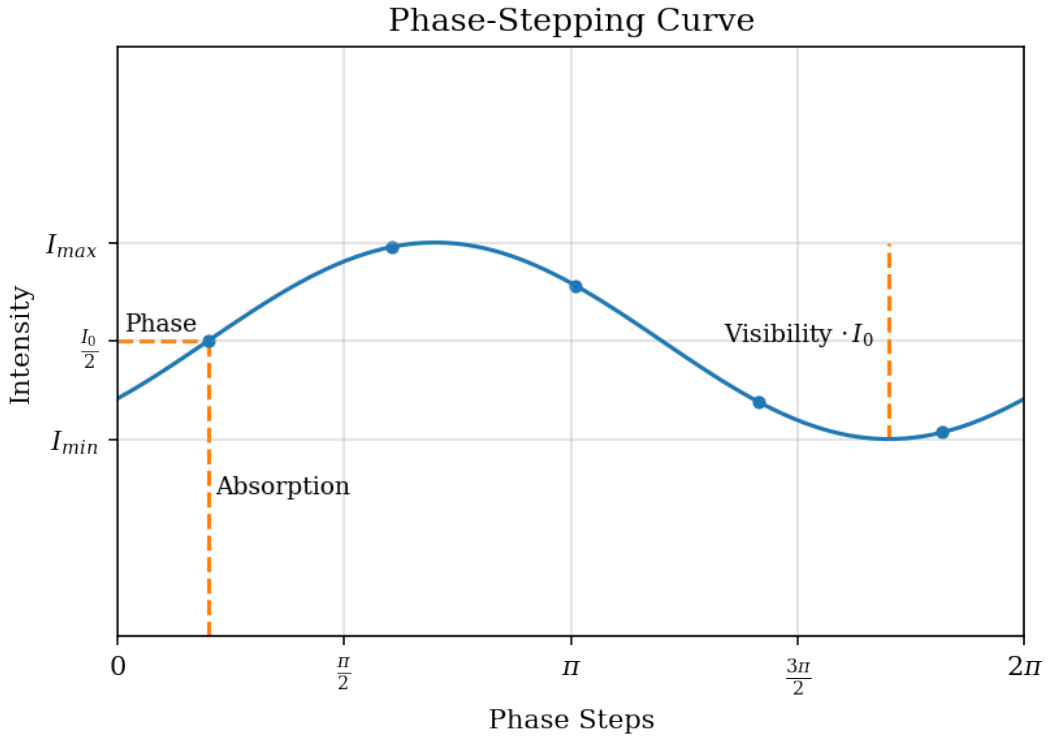
Fig. 5: The parameters absorption, phase and visibility are shown schematically. The absorption represents the mean photon count over various phase steps of the analyzer grating G_2. The phase represents the phase offset to zero and the visibility is the difference between the highest and lowest point of the curve

Dual Phase Grating Interferometry

As mentioned in *Talbot-Lau Grating Interferometry*, conventional TLGI suffer from poor dose efficiency due to the employment of absorption gratings and changing the auto-
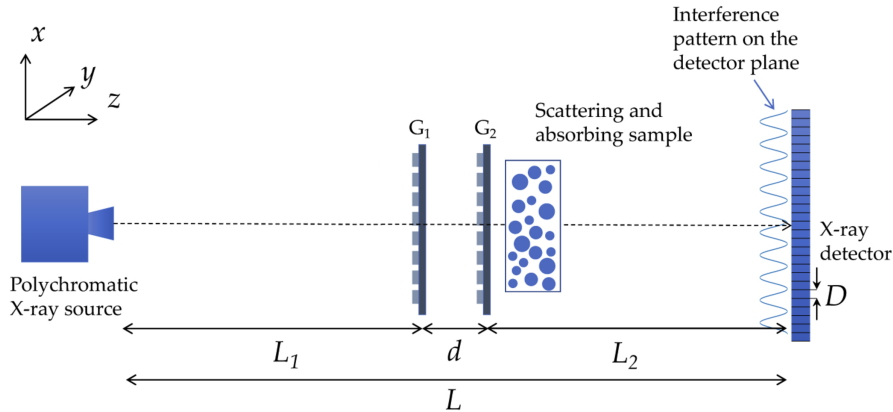
Fig. 6: Schematic representation of a dual phase interferometer as used in this study. G_1 in combination with G_2 generates a directly resolvable fringe with period p_f. (Adapted and Modified from [46])

correlation length of a given setup poses a fair number of challenges. As recent as 2017 Kagias et al. demonstrated an alternative by employing of two phase gratings instead to perform absorption, DPC and tunable dark-field imaging[47]. The source directly illuminates the first phase grating G_1, which leads to formation of a Talbot carpet. The resulting intensity pattern hits G_2, generating a large pitch fringe modulation at the detector plane. This fringe's pitch p_f can be designed such that it can be resolved directly without any aliasing effects by the detector in use. Generally speaking the G_1 and G_2 need to heave slightly different periods to generate a large pitch fringe at the detector plane. However, by operating in a cone beam geometry one can use identical gratings and employ the resulting geometric magnification to achieve this period difference. In case of identical grating periods $p = p_1 = p_2$ of the two phase gratings, the fringe period p_f is given by

$$p_f = \frac{Lp}{2d} .$$ (10)

The resolved fringe can then be used to quantify absorption, DPC and dark-field signal either via phase stepping of G_2 or analysis of the raw fringe directly. In either case, the detector must be able to resolve the fringe directly.

Such a dual phase setup brings with it a number of advantages. First, no absorption gratings are required in its operation, providing a much higher dose efficiency. The auto-correlation length

$$\xi_{DP} = \frac{\lambda L_1 d}{p_1 L}$$ (11)

21

can easily be adapted by changing the inter-grating distance d between G_1 and G_2 allowing for tunable dark-field imaging and operation close to a parallel beam geometry further simplifies image evaluation as almost no change in geometric magnification occurs. A schematic representation of a dual phase setup is given in Fig. 6.

Aim of this thesis

Dark-field imaging of human lungs is a promising, X-Ray based technique to improve diagnostic performance of respiratory disease especially in case of early onset diagnostics without raising the effective dose in a significant level. First clinical trials done by Pfeiffer et al. establish the working principle in humans subjects and demonstrate the methods strengths with respect to its sensitivity towards changes in the unresolved microstructure of the lung tissue. Although dark-field imaging of the lung as been under investigation for close to ten years by now, to the best of our knowledge, no detailed investigation regarding the behavior of the lung's dark-field signal with respect to variation of the auto-correlation length ξ has been undertaken. Only a few distinct values have been reported[14,15]. The experiments and data analysis contained in this thesis were performed with the aim to establish the means to cleanly handle, inflate and image fresh porcine lungs over a wide range of auto-correlation lengths using three different imaging setups. Starting point was a preexisting wide-field-of-view grating interferometry setup and a theoretical study of lungs and their anatomy. Preliminary handling and inflation tests were performed to assess the required needs. These results were the starting point to design a vacuum chamber allowing for lung inflation which was used in all subsequent imaging procedures. It formed the foundation for scanning lungs at multiple auto-correlation lengths on two Talbot-Lau GI and on a recently installed dual-phase interferometer generating the data to characterize $\Sigma(\xi)$ of porcine lungs, estimate the size of structure contributing to $\Sigma(\xi)$ as well as allowing to estimate a working ξ-range for an interferometer capable of handling lungs of human proportions.

Materials and Methods

Sample Materials

Porcine Lungs

Fresh porcine lungs were ordered through the veterinary department and obtained directly from the slaughterhouse of Zurich, Switzerland. As the pigs in question were destined to be slaughtered regardless of our study, no further ethics approval was necessary. In Switzerland, lungs fall into the category "K1" and are thus considered "risk

materials". Materials of category "K1" are banned from entering the food-cycle and have to be burned. This was ensured by disposing the samples at the cadaver collection facility after experiments, provided by each municipality in Switzerland. Over the course of this study approximately 14 porcine lungs have been acquired and used for experimenting and imaging.

PMMA Microspheres

Six PMMA (Polymethylmethacrylat) microspheres samples were obtained from Cospheric LLC (Santa Barbara, California 93160, USA) containing microspheres with various size ranges as following: $20\,\mu m$ to $27\,\mu m$, $45\,\mu m$ to $53\,\mu m$, $63\,\mu m$ to $75\,\mu m$, $180\,\mu m$ to $212\,\mu m$, $225\,\mu m$ to $300\,\mu m$ and $425\,\mu m$ to $500\,\mu m$. These sizes were chosen such, that they clearly cover the size of alveolar structures in lungs. PMMA microspheres can pose a health risk if they come in contact with eyes, are ingested, inhaled or otherwise introduced to the body. The spheres were generally stored inside a sealed box while contained in individual airtight glass vials.

While these micro-sphere samples possess a comparable microstructure as the one found in lungs, though clearly much more isotropic, they differ from lungs in a major aspect. The spheres effectively represent the inversed material-phase of the lungs, as the spheres are made of PMMA and the spaces in between are filled with air. In lungs, however, the alveoli are filled with air and the surrounding spaces are filled with tissue. To correct for that inverse nature of the material-phases a ideal spherical packing order was assumed for the PMMA-microspheres with an average packing density of 0.74. The R values of the PMMA microspheres were thus multiplied by a correction factor of 2.84 to correct for the additional absorption, allowing for direct comparison.

Lung Preparation and Inflation

Lungs in humans and in pigs get inflated by a negative pressure surrounding them and forcing the air through the trachea into the lungs. It is as well possible to inflate them by applying a pressure to the trachea and sealing major holes to maintain a constant positive pressure inside the airways. For either case, a tight seal to the trachea is required and thus the preparation of the lungs was the same regardless of inflation method.

After obtaining the lungs (including the larynx still connected to the trachea) from the local slaughterhouse in the morning, they were washed on the outside with water and inspected for visible damage. Most lungs displayed minor or major cuts/injuries resulting from the butchering process providing an escape way for air if pressurized. Subsequently, the trachea was severed about halfway between the larynx and the tracheal bifurcation. Depending on the condition of the lungs, either the whole lungs were used or the more
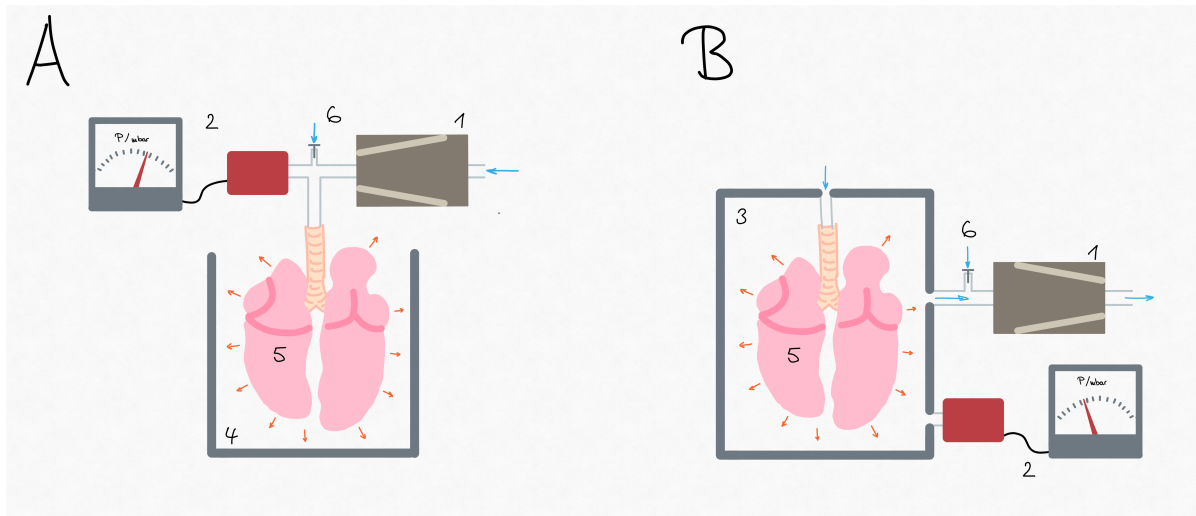
Fig. 7: Schematic representation of the configurations used to inflate porcine lungs. A) By applying a positive pressure . B) By pulling a vacuum surrounding the lungs. 1: Air pump used to over/under pressurize the volume; 2: Absolute pressure sensor; 3: Air-tight container allow for establishing a vacuum around the lungs; 4: Open container in which the lungs were placed; 5: the pig lungs; 6: A valve used to regulate the effective pressure.

damaged side was cut off directly at the primary bronchi. The open airway was then sealed by means of a clamp providing a tight seal needed for inflation.

A tight seal to the trachea was achieved by inserting a plastic tube of 8/6 mm diameter into the trachea and fixing it with three zip ties around the outside. Commercial tracheal tubes were examined for this purpose as well but did not provide any advantage over the simpler and more efficient plastic tube.

Inflation by Pressurizing the Airways

For inflation via pressurization of the airways, the tracheal tube was connected to a pump and a pressure of ca. $+0.03$ mbar was applied in a controlled manner via a open valve and a absolute pressure sensor (PCR 280, Pfeiffer Vacuum GmbH, Asslar, Germany). The lungs were then placed in a plastic container to allow for imaging. This method was employed early on to get a good understanding on the lungs and how to handle them.

Inflation by Surrounding Vacuum

Fig. 8: The inflation chamber. The orange-brown Kapton foil is used to seal the chamber along the beam axis achieving minimal beam interaction.

Under *in vivo* conditions the lungs get inflated by a reduced surrounding pressure forcing the air into the lungs. To allow for inflation by a surrounding vacuum an air-tight container was constructed which allows for imaging without affecting the image. Inspired by [48], such a vacuum chamber was designed and built in-house and is shown in Fig. 8. It allows to mount the lungs fitted with the tracheal tube into the chamber, and connecting it to the surrounding atmosphere via the inlet in the chamber's lid. Once the lid was sealed and secured a vacuum was applied by means of an external pump. The pressure was monitored via an absolute pressure sensor (PCR 280, Pfeiffer Vacuum GmbH, Asslar, Germany) and controlled via a valve. To provide minimal interaction with the beam, windows were introduced along the imaging axis and sealed with 0.075 mm thick Kapton foil (Dupont, Wilmington, DE, USA) which was securely glued to the frame with Araldite Standard two-component glue (Huntsman Corp., The Woodlands, TX, USA).

Fig. 9: Mounting of a left porcine lung for imaging. *Left:* The right main bronchus is seal of by a clamp (green). *Center:* The lung is fixed to the lid of the vacuum chamber with zip ties. The tube is securely fixed into the trachea and connected to the inlet in the lid. *Right:* The left porcine lung inflated inside the vacuum chamber at -30 mbar.

Imaging

Three different imaging setups were used during this study. Two classical Talbot-Lau grating interferometer (TLGI) and a dual-phase interferometer which in combination provided access to auto-correlation lengths in a range between 77 nm and 5.2 μm.

Inverse Geometry Setup

This setup was a wide-field-of-view cone beam grating interferometer with inverse geometry. While conventional grating interferometer have their G_1 grating closer to G_2 than to G_0 an inverse geometry requires exactly the opposite. Practically speaking, an inverse geometry setup can be seen as a conventional geometry with inversed beam direction. The design energy was 46 keV. The total length of the setup was 996 mm, G_0, G_1 and G_2 were placed at 100 mm, 388 mm and 983 mm, respectively. All distance are referenced to the position of the focal spot as 0 mm. The distances correspond to the first Talbot order. The X-Ray source used was a Comet MXR-225HP/11 (Comet Group, Flamatt, CH). It has a focal spot size of $0.4 \, \text{mm}^2$ run with 70 kVp at 10 mA and the conical photon field fully covered the sensitive area of the detector

The absorption gratings G_0 and G_2 were produced by means of the LIGA process by Micro Works (Karlsruhe, DE) out of gold on a graphite substrate. G_1 was produced by

26
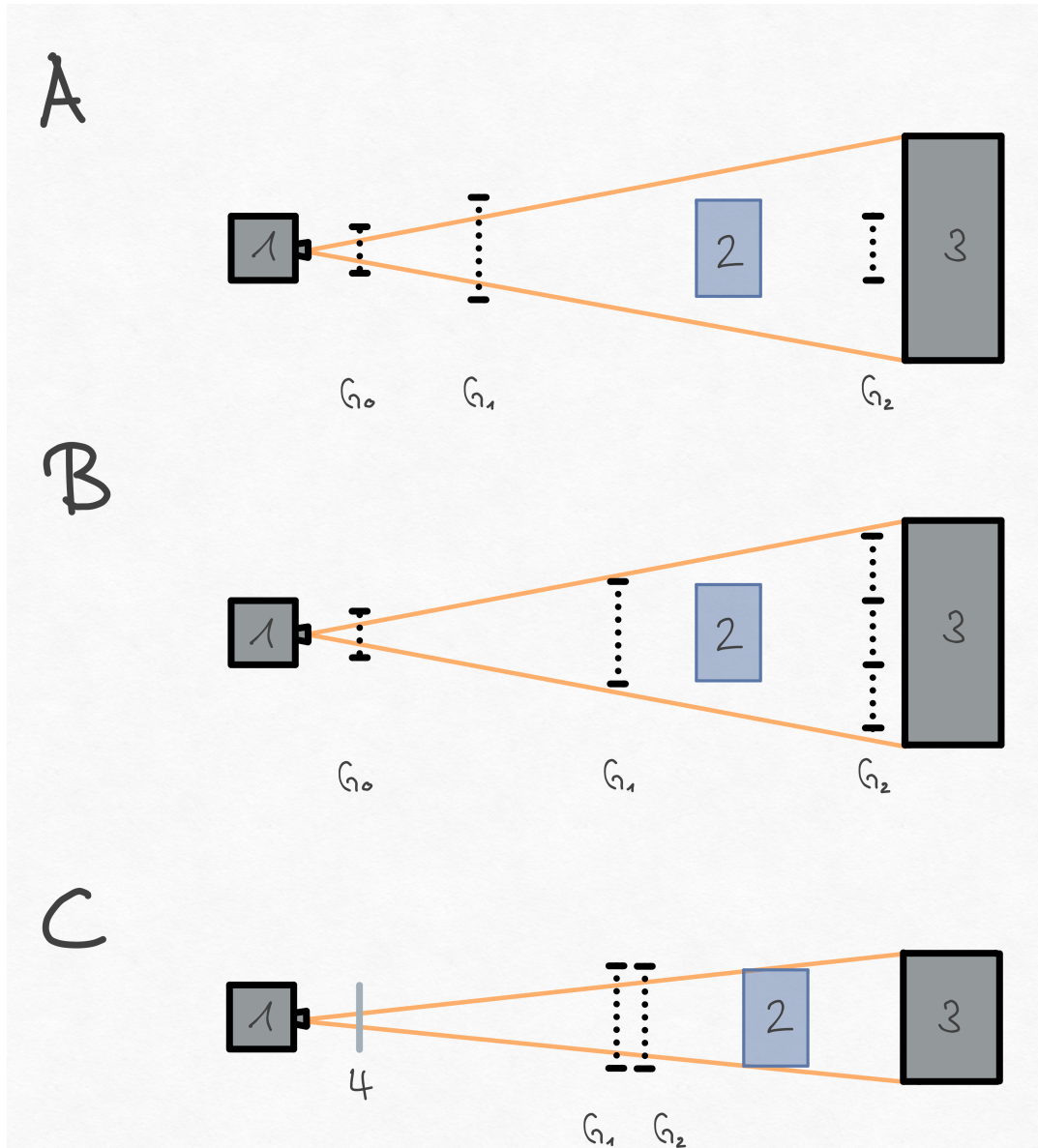
Fig. 10: The three setups used during this work. The conceptual sketches are not to scale and only intended for illustrative purposes. A) The inverse geometry Talbot-Lau GI. B) The symmetric geometry Talbo-Lau GI. C) The dual-phase GI. 1: The X-Ray source; 2: The sample position in the beam (variable in A & B); 3: The detector; 4: Aluminium plate (3 mm) for filtering the beam.

means of etching a silicon substrate. To accommodate the conical beam geometry the gratings were bent along the vertical axis after fabrication to ensure perpendicularity to the incoming photons across the entire field of view. The gratings are specified in detail in Table 2. G_0 was stepped by a P-841.6 piezoelectric-motor (Physik Instrumente GmbH & Co. KG, Karlsruhe, DE) with an accuracy in the order of $\sim 1\,nm$. With step sizes in the order of $0.8\,\mu m$ used for G_0, this was considered to be sufficiently accurate. The sample stage is positioned in between G_1 and G_2 and consisted of a vertical axis and a mounting stage capable of hosting a variety of different sample containers. The vertical axis additionally allowed for vertical scanning by stitching to increase the field of view in vertical direction. To allow for multiple auto-correlation lengths (ξ_1), the entire sample stage was moved along the beam axis between the two gratings, resulting in a range of possible auto-correlations lengths $\xi_1 \in [0.66 - 1.36]\,\mu m$. Note, that this process affects the geometric magnification of the sample due to the conical beam geometry, which in turn affects the effective resolution. In this setup, magnifications between 1x and 2.5x resulted.

For detection behind G_2 a prototype detector by the name Santis (Dectris, Baden-Daettwil, CH) was used. This detector is a direct-conversion photon-counting device with Cadmium Telluride (CdTe) as active medium for detection. It has an intrinsic resolution of 256×3096 isotropic $75\,\mu m$ pixels. Furthermore, it features a dual energy photon counter with adjustable energy thresholds. This allows to vary the bandwidth of X-Rays contributing to the measurement (from near monochromatic to full spectrum).

Gratings	Absorption I (G$_0$)	Phase (G$_1$)	Absorption II (G$_2$)
Material	Gold	—	Gold
Substrate	Graphite	etched Silicon	Graphite
Period / [μm]	4.8	6.47	9.92
Lamella Height / [μm]	150	59	150
Duty Cycle	0.5	0.5	0.5
Dimensions (L × W) / [mm × mm]	45 × 10	80 × 17	80 × 40

Table 2: Specifications of all three gratings (G$_0$, G$_1$, G$_2$) used in the inverse geometry setup.

Symmetric Geometry Setup

The second setup was a wide-field-of-view cone beam grating interferometer with symmetric geometry. Symmetric geometries place G_1 exactly in the center between G_0 and

Gratings	Absorption I (G$_0$)	Phase (G$_1$)	Absorption II (G$_2$)
Material	Gold	—	Gold
Substrate	Graphite	etched Silicon	Graphite
Period / [μm]	4.2	4.2	4.2
Lamella Height / [μm]	180	60	180
Duty Cycle	0.5	0.5	0.5
Dimensions (L × W) / [mm × mm]	80 × 60	203 × 75	80 × 60

Table 3: Specifications of all three gratings (G$_0$, G$_1$, G$_2$) used in the symmetric geometry setup.

G$_2$ and have the advantage that they are the shortest for a given period p_1 of G$_1$. Additionally, G$_0$ and G$_2$ have the same period $p_0 = p_2$ and the same production techniques can be used, streamlining the process. The design energy of the symmetric setup was 46 keV and total length was 1636 mm. G$_0$, G$_1$ and G$_2$ were placed at 100 mm, 818 mm and 1636 mm, respectively. G$_0$ and G$_2$ are made of gold on a graphite substrate while G$_1$ is made from etched silicon. The absorption gratings were again produced by Micro Works (Karlsruhe, DE) and the phase grating was produced *in house*. All gratings are specified in detail in Table 3. The same source (Comet MXR-225HP/11, Comet Group, Flamatt, CH) as well as the same detector (Santis Prototype, Dectris, Baden-Daettwil, CH) as in the inverse geometry setup were used and consistently run with 70 kVp at 10 mA. The distances correspond to the fifth Talbot order. By using three identical G$_2$ next to each other and the extra-wide G$_1$ a total field of view of ca. 240 mm × 15 mm was achieved.

Dual-Phase Setup

The dual-phase setup used in this work had a total length of 2800 mm while also being of symmetric geometry, such that the source to G$_1$ distance resulted in 1400 mm. The inter-grating distance d was possible to adjust via a linear stage, on which G$_1$ was mounted, in steps of 1 mm. The sample was placed between G$_2$ and the detector. First, the same detector as in the other two interferometer (Santis Prototype, Dectris, Baden-Daettwil, CH) was used with a resolution of 75 μm and the ability to for dual-energy thresholds (for details see *Inverse Geometry Setup*). To increase the range of accessible auto-correlation lengths (e.g. being able to resolve higher pitched fringes) the CdTe detector was exchanged for a CCD camera (SCX:4300, Teledyne Princeton Instruments, Trenton, New Jersey, USA) with an isotropic 24 μm pixel size. It features an intrinsic resolution of 2084 x 2084 pixels providing a field of view of 120 × 120 mm. As scintillator

material, Gadox ($Gd_2O_2S:Tb^{3+}$) was used with a peak sensitivity at 17 keV while the design energy of this dual-phase interferometer is 30 keV. The source used for the dual-phase setup was a Hamamatsu L10101 (Hamamatsu Photonics, Hamamatsu, Japan) consistently run with 70 kVp at 200 µA.

Gratings	Phase I (G$_1$)	Phase II (G$_2$)
Material	—	—
Substrate	etched Silicon	etched Silicon
Period / [µm]	1.2	1.2
Lamella Height / [µm]	40	40
Duty Cycle	0.5	0.5
Dimensions (L × W) / [mm × mm]	75 × 75	75 × 75

Table 4: Specifications of both phase gratings (G$_1$, G$_2$) used in the dual-phase setup.

The identical phase gratings (G$_1$, G$_2$) were produced *in-house* by Zhitian Shi by means of Silicon etching. As this setup was operated close to parallel beam geometry, no bending of the gratings was required. The gratings are specified in detail in Table 4.

Timeline and Imaging Protocol

All lungs used in this study were collected around 8 am in the morning, transported to the lab, prepared and imaged on the same day. Preparation took roughly 1.5 h, allowing to start imaging around 11 am. The imaging process, depending on the requirements, took up to maximal 9 h. The vacuum chamber ensured consistency over these prolonged imaging procedures in terms of pressure, humidity and location.

Measurement at a single auto-correlation length on the TLGI adhered to the following protocol: To enlarge the field of view, vertical scanning and stitching was used. For each slice, five phase-steps with an exposure time of 5 s were taken leading to 25 s per slice. Flat-field images were recorded pre- and post- sample scanning and averaged before used for flat-field corrections according to Eq.9. Each vertical slice was signal-retrieved individually and stitched in post processing for each contrast channel. On the dual-phase GI an exposure time of 20 s was used and a flat-field image was only taken at the start of the measurement. It was operated only in single-shot mode.

Inflated porcine lungs were imaged in parallel with non-inflated porcine lung tissue and multiple tubes of PMMA spheres, fitted into the same field of view. A representative configuration used for imaging is shown in Fig. 11.

This configuration was imaged at auto-correlation lengths between 0.8 μm to 3.6 μm, as the size of the vacuum chamber put a limit to the accessible range on the symmetric Talbot-Lau GI. The PMMA spheres and a piece of non-inflated lung tissue, however, were imaged on the full range available providing additional data points at auto-correlation lengths between 3.6 μm to 5.2 μm. Fig. 12 to 16 show the image results of inflated lung scans at $\xi = 0.8$, 1.99 and 3.64 μm. At these three auto-correlation lengths, scans making use of the full vertical range were performed, taking 22 vertical slices in steps of 10 mm. At all other positions along the beam axis, in between those three, a reduced field of view (FOV) was scanned, using 8 vertical slices. The red line in Fig. 12 indicates the upper limit of the reduced FOV scans. Vertical slices were signal retrieved and stitched during post-processing, returning large FOV images as shown in Fig. 12 to 16. The same regions of interest were evaluated at each auto-correlation length. They are indicated by colored circles in Fig.12 to 14 and correspond to the colors used later on in Fig. 17 & 18, where detailed results of the dark-field measurements done on the symmetric Talbot-Lau GI are presented.

Data Analysis and Statistics

All data analysis, image processing and statistics has been performed in Python 3.8 under Anaconda 1.10.0. Several packages and modules were used for Python, including but not limited to matplotlib[49], numpy and scipy[50].

Results

The process to retrieve quantitative dark-field images of inflated porcine lungs can be divided into two main phases. First, the means to acquire, handle/prepare, inflate and image porcine lungs had to be established. Afterwards a series of porcine lungs was imaged in a repeatable manner on the conventional Talbot-Lau interferometer as well as on the dual-phase interferometer. Details on the inflation methodology and setup can be found in *Lung Preparation and Inflation*.

Imaging on the Symmetric Talbot-Lau GI

The final data presented in this thesis results from two different specimen of porcine lungs which to the best of our knowledge were healthy and representative of adult pigs. They were imaged by using the designated vacuum chamber with a negative pressure of −30 mbar acting on them. It was found that initial inflation requires lower pressures (down to −60 mbar) than usually present under *in-vivo* conditions. Once the lungs

31
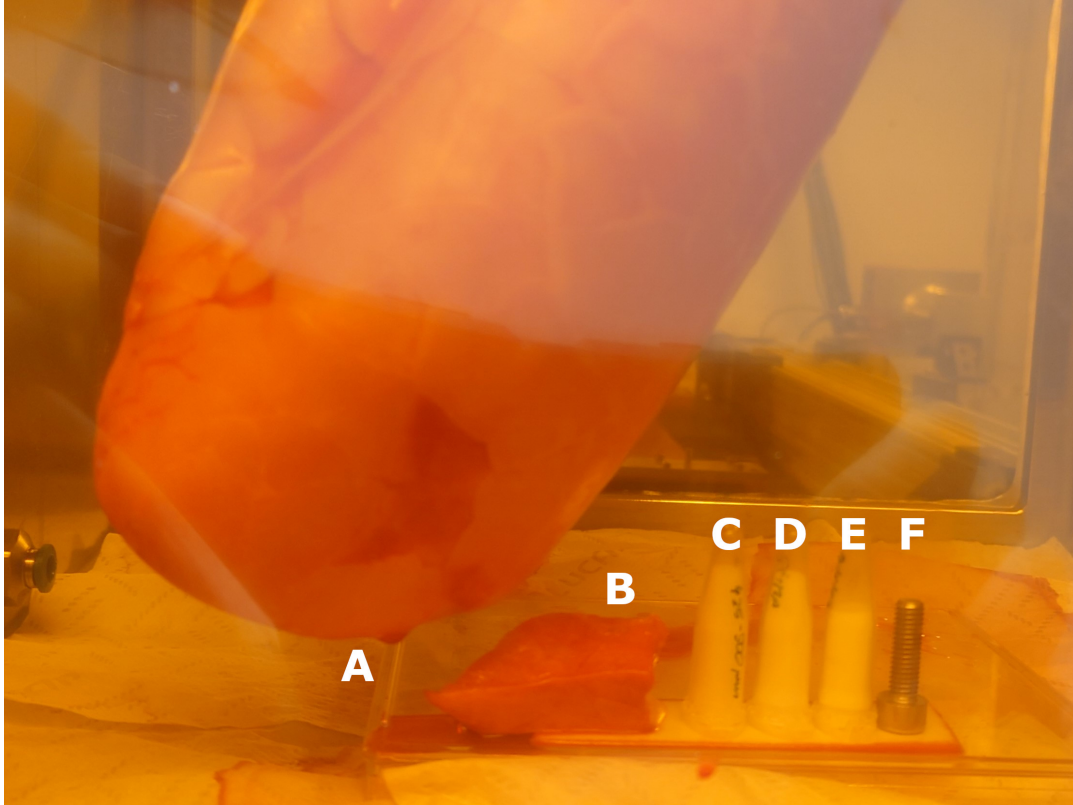
Fig. 11: Point of View from G_2 of the symmetric TLGI into the vacuum chamber. A) Apical segment of the inflated left porcine lung. B) A piece of non-inflated porcine lung tissue. C, D, E) Falcon tubes containing PMMA spheres of 425 to 500, 180 to 212 and 20 to 27 µm, respectively. F) A M4 steel screw (4 mm in diameter) as reference marker.

appeared completely inflated, the pressure was readily reduced to physiological levels and the lungs were left idly for 1 h at -30 mbar to arrive at a steady-state of inflation. Falcon tubes containing PMMA spheres were imaged alongside the porcine lungs as reference samples of comparable feature size. Fig. 11 shows the sample configuration used for imaging.

The retrieved absorption images in Fig. 12 nicely highlight the internal organization of the lung's airways. Furthermore, no difference in terms of absorption can be seen for the Falcon tubes containing different PMMA spheres, as expected. The dark-field images in Fig. 13 demonstrate several things: First, it is apparent that at auto-correlation lengths between 0.8 µm to 3.6 µm our setup allowed to capture the effect of small angle scattering by the lung tissue as well as by all three PMMA sphere samples. One can see a clear increase in dark-field signal with an increase in auto-correlation length, again, as expected. Second, the differences in the dark-field signal between the different

PMMA spheres highlights not only the strength of dark-field contrast in terms of providing information about the unresolved micro-structure of a sample but simultaneously allows to characterize an approximate feature size of porcine lungs generally contributing to the dark-field signal. Finally, the dark-field images show dominant repeating patterns, increasing proportionally with the auto-correlation length. It was found that these patterns originate in the shape of the X-Ray wavefront under flat-field conditions (see Fig. 15) and can practically be attributed to the saturation of the signal as further explained in *The Manifestation of Signal Saturation*. Normalizing the dark-field (Σ) images by dividing through the corresponding absorption (Γ) returns the thickness independent R-values/image.

$$R = \frac{\Sigma}{\Gamma} = \frac{-\ln(\frac{V}{V_0})}{-\ln(\frac{I}{I_0})} = \frac{\epsilon t}{\mu t} = \frac{\epsilon}{\mu}, \tag{12}$$

where μ is the linear attenuation coefficient and ϵ is the dark-field extinction coefficient defined analogously. Under normal conditions (e.g no saturation) it allows for direct comparison of the dark-field signal between samples of different thicknesses t, effectively representing a t independent scattering power of a give sample material at a given auto-correlation length. One expects an increase in R by increasing the auto-correlation length, same as for the dark-field. In Fig. 14 a consistent increase in R from left to right is only observed for the thinnest areas of the lungs (edges and apical ends) as well as for the PMMA spheres, due to dominating saturation effects.
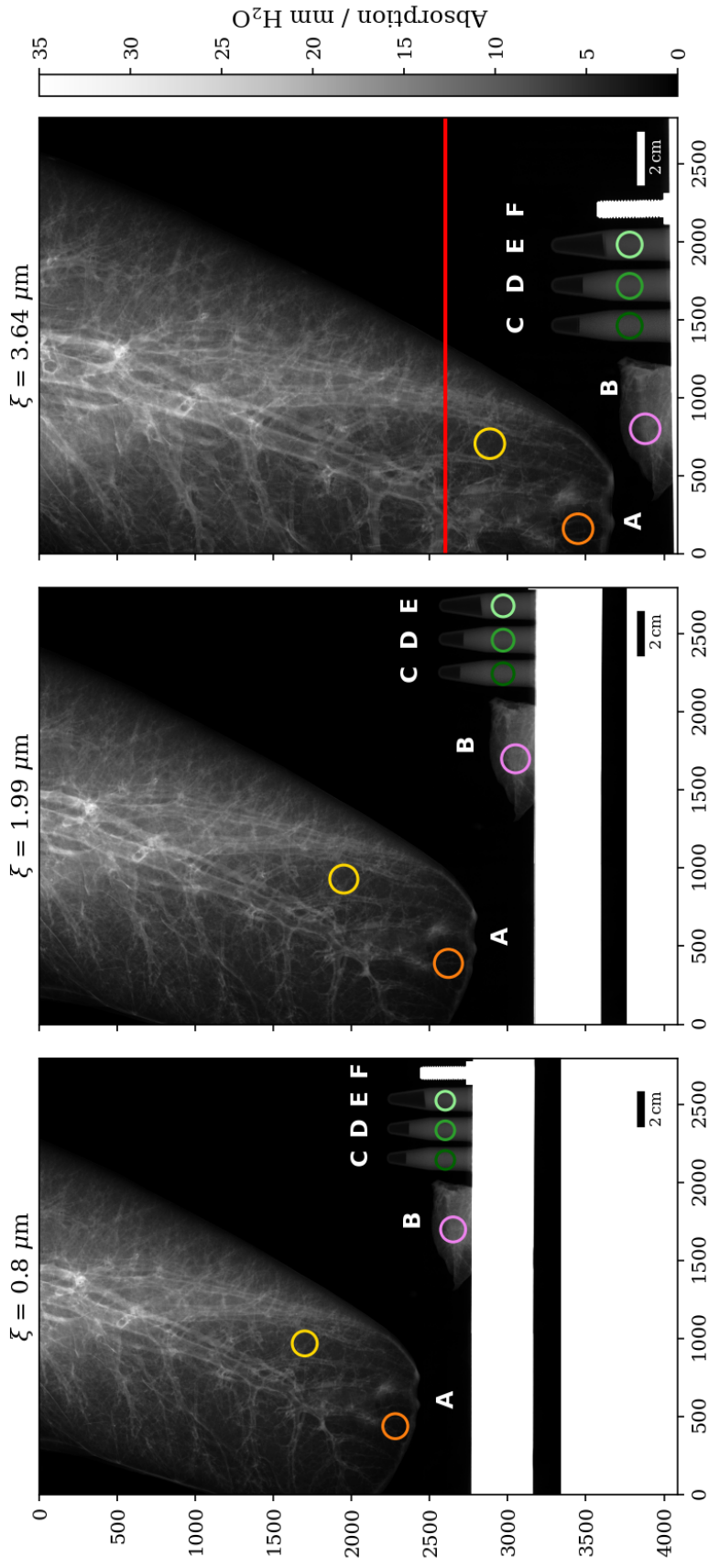
Fig. 12: Retrieved absorption (Γ) images in units of mm H_2O of A) inflated porcine lung tissue, B) non-inflated porcine lungs, C-D) PMMA spheres of sizes 425 to 500, 180 to 212 and 20 to 27 µm, respectively, and F) a M4 steel screw (4 mm in diameter) as reference marker, ordered by increasing auto-correlation length. Exposure time was 5 s per vertical slice for a total of 22 slices, later combined by stitching. Circles indicate evaluated ROI, colors correspond to Fig. 17 & 18. For all remaining measurements only the area below the indicated red line was imaged.
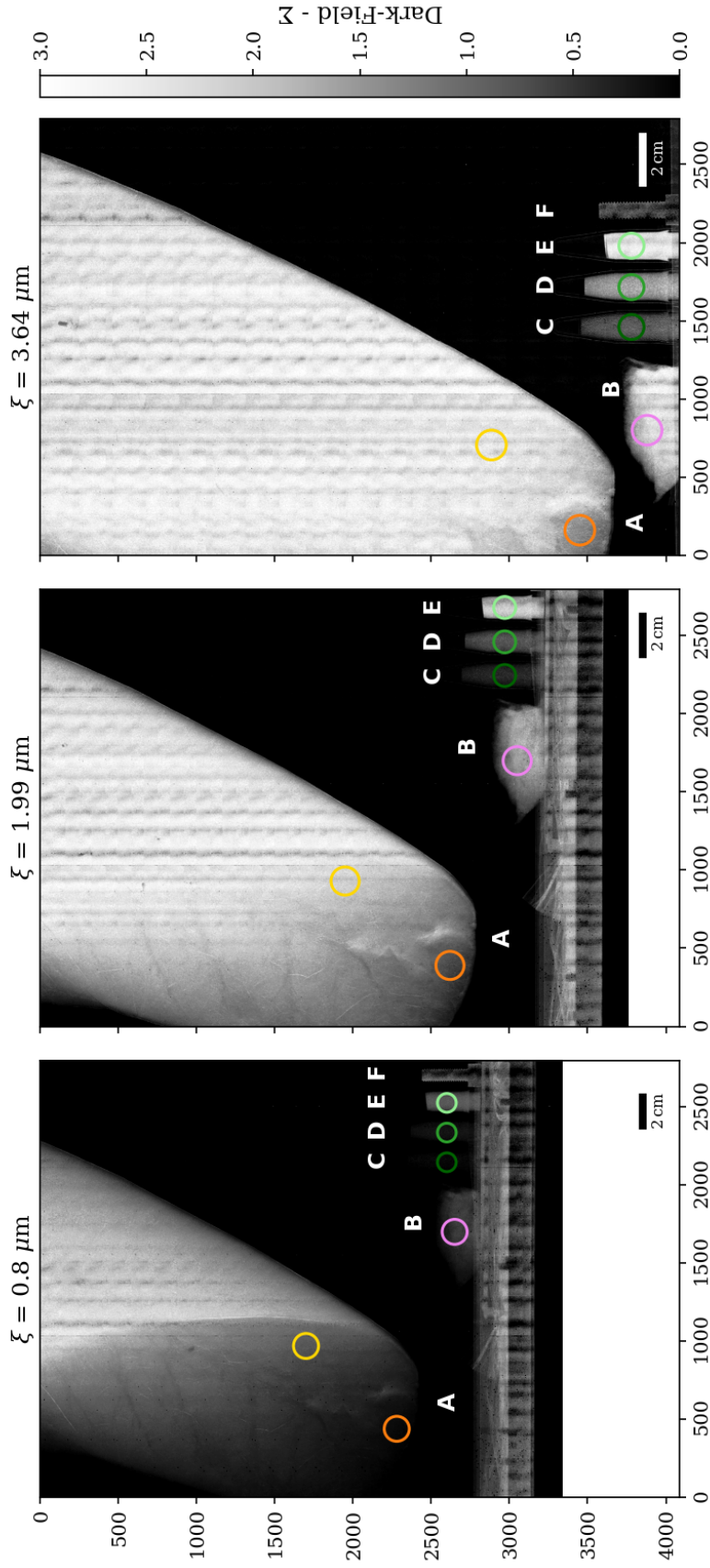
Fig. 13: Retrieved dark-field (Σ) images of A) inflated porcine lungs , B) non-inflated porcine lung tissue, C-D) PMMA spheres of sizes 425 to 500, 180 to 212 and 20 to 27 µm, respectively, and F) a M4 steel screw (4 mm in diameter) as reference marker, ordered by increasing auto-correlation length. Exposure time was 5 s per vertical slice for a total of 22 slices, later combined by stitching. Circles indicate evaluated ROI, colors correspond to Fig. 17 & 18. Note the increase in signal with increasing auto-correlation length. The repeating patterns, appearing at larger auto-correlation lengths, result from signal saturation (see *The Manifestation of Signal Saturation*).

35

Fig. 14: Retrieved R (Σ/Γ) images of A) inflated porcine lungs , B) non-inflated porcine lungs, C-D) PMMA spheres of sizes 425 to 500, 180 to 212 and 20 to 27 µm, and F) a M4 steel screw (4 mm in diameter) as reference marker, ordered by increasing auto-correlation length. Exposure time was 5 s per vertical slice for a total of 22 slices, later combined by stitching. Circles indicate evaluated ROI, colors correspond to Fig. 17 & 18. Correcting the dark-field signal with absorption allows to obtain a thickness independent signal in areas where no saturation effects are present (see *The Manifestation of Signal Saturation*).

The Manifestation of Signal Saturation

Phenomenologically speaking, the saturation of the dark-field signal can be easily understood by the following example: Assume you are taking a classical absorption image of an object, for example a steel plate, with the aim to determine its thickness. Under suitable conditions you will be able to detect plenty of photons with your detector on the other side of the object according to the Lambert-Beer law. Let's now go ahead and increase the objects thickness. The absorption will increase and therefore your photon counts on the detector will decrease. The estimated thickness will go up. From a certain thickness on on-wards, however, the detected photon counts won't be high enough to distinguish them from noise inherent to your measurement. At this point the only thing you can infer from your measurement is, that the plate is thicker than a specific maximal thickness.

Wavefront of the Symmetric Talbot-Lau GI
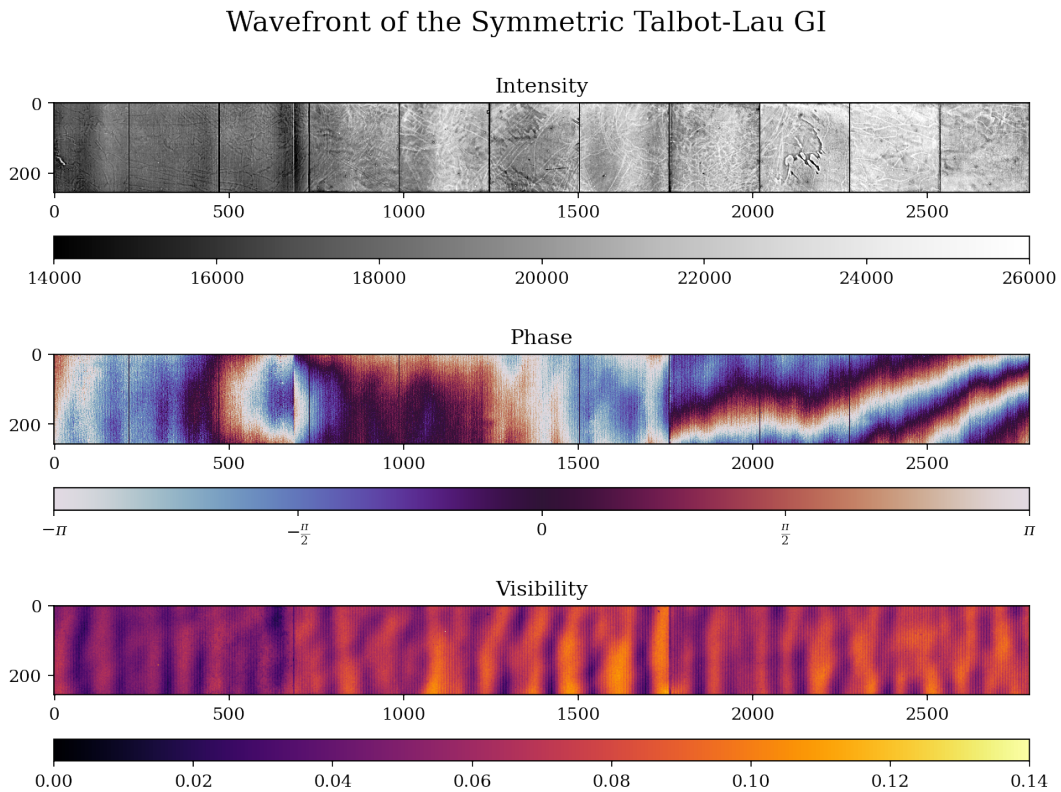
Fig. 15: The wavefront as recorded under flat field conditions. *Top:* The Intensity profile - visible structures result from the Cadmium Telluride crystals used in the detector. *Center:* The phase profile. *Bottom:* The visibility profile - the variations of the visibility seen here over the complete field of view reappear in a reconstructed dark-field image if the signal saturates.

Things behave quite similarly in terms of the dark-field signal. A sample scatters, leading to visibility loss. If we continuously increase the thickness of the sample, the visibility decreases until it is close to, but never truly zero - in the given context it means that the fringe of our interferometer blur's by such a degree, that we can no longer differentiate between pure noise and actual signal. Instead of increasing the sample's thickness, we can increase the auto-correlation length ξ analogously which makes the whole setup more sensitive towards the dark-field signal. This will be true as long as we are operating in a regime where $\xi << D_{true}$ with D_{true} being the true feature size in a sample. This was certainly the case for all measurements performed during this study. As such, the same sample will lead to more signal and eventually saturation before the peak in dark-field signal is reached.

This is why we observed the repeating patterns in the dark-field images (see Fig. 13) and subsequently in the R images (see Fig. 14). As the calculation of the dark-field signal uses the flat field visibility V_0 at its foundation, it is bound to reappear once the visibility reaches its minimal value V_{Noise}

$$\Sigma = -\ln\left(\frac{V_{Noise}}{V_0}\right).$$
(13)

Looking at a single pixel of our image, the detected counts of incoming X-Rays follows Poisson's statistics

$$P(n;\mu) = \frac{\mu^n e^{-\mu}}{n!},$$
(14)

where μ equals the mean value and n is the number of occurrences. It can be shown that $\sigma = \sqrt{\mu}$, allowing to easily calculate the standard deviation of our photon counts. The visibility is commonly defined as

$$V = \frac{I_{max} - I_{min}}{I_{max} + I_{min}}$$
(15)

and in case of a complete loss of visibility (aka maximal scattering) should amount to zero for which the dark-field signal is effectively no longer defined due to its logarithmic nature. In practice, V will never equal zero but the phase-stepping curve will be defined by noise rather than by the desired interference pattern. If we can no longer differentiate

reliably between I_{min} and I_{max} the signal is saturated. We can formulate a saturation score

$$S_{Sat} = \frac{2\sqrt{I_{max}}}{I_{max} - I_{min}}, \tag{16}$$

allowing us to assign each pixel a saturation value. Theoretically, if the score exceeds 1 the pixel is saturated. In practice, the effect of saturation manifests itself earlier and in this study an empirical threshold of 0.78 was used for classification of pixels as saturated. The saturation map of the measurements shown in Fig. 12 to 14 is shown in Fig. 16.
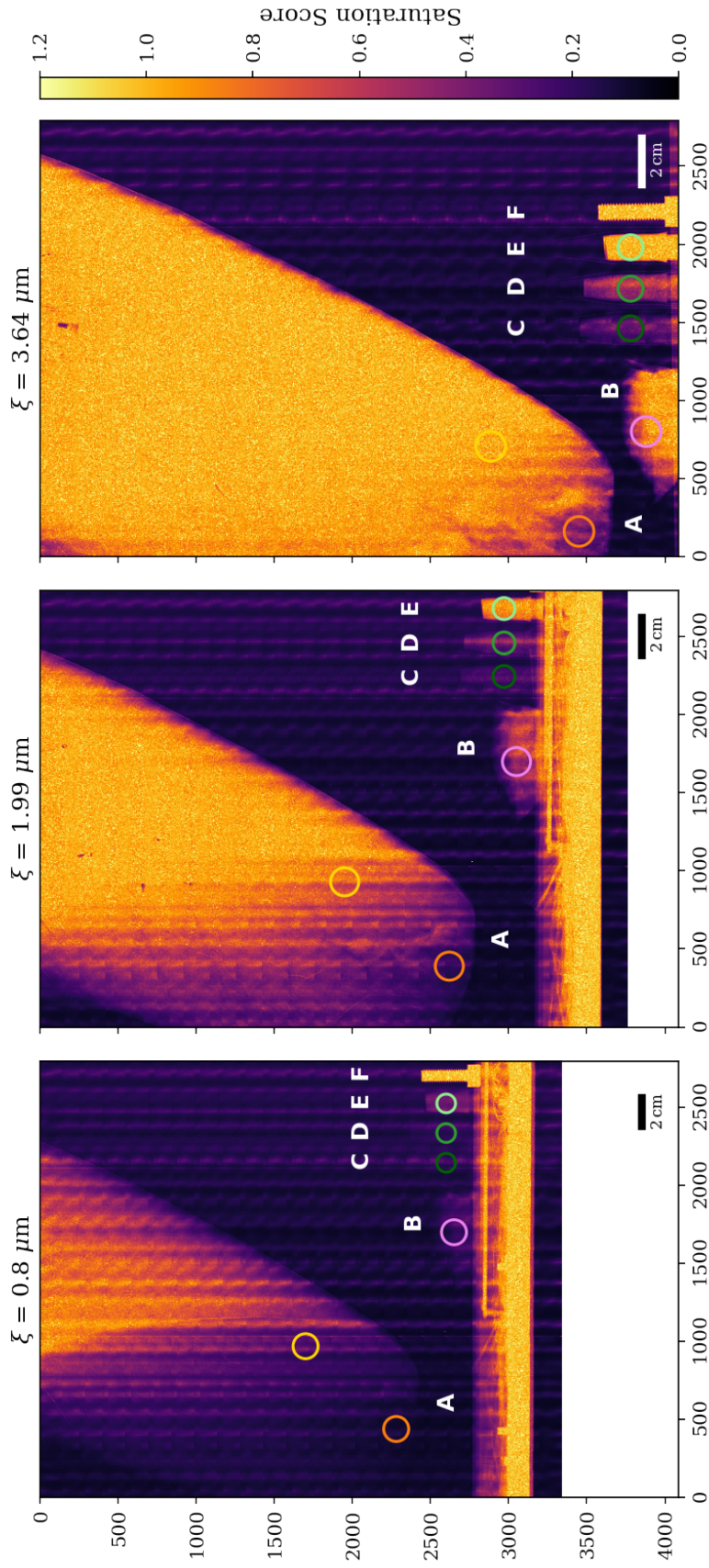
Fig. 16: The calculated saturation map for inflated porcine lungs based on the phase-stepping curve. B) non-inflated porcine lung tissue, C-D) PMMA spheres of sizes 425 to 500, 180 to 212 and 20 to 27 μm, and F) a M4 steel screw (4 mm in diameter) as reference marker, ordered by increasing auto-correlation length. Exposure time was 5 s per vertical slice for a total of 22 slices, later combined by stitching. The increase in saturation with increasing auto-correlation length is clearly visible in both lung samples as well as in the smallest PMMA spheres.

The Dark-Field Signal as a Function of the Auto-Correlation Length

All scans combined, a total of 41 and 26 measurements were collected for each PMMA sphere sample and each porcine lung sample, respectively. Fig. 17 & 18 show those measurement series in detail, corresponding to the indicated ROIs in Fig. 17. Values considered saturated by their saturation score are marked with red edges. Measurements of the PMMA spheres have been corrected for the inverted material phases by a factor of 2.84. In case of the dark-field signal, the respective sample thickness is a major factor, as such they are reported here in $mm\,H_2O$ equivalents. All PMMA sphere measurement series were recorded at $4.8\,mm\,H_2O$ equivalent thickness. The series 'Lung inflated 1' and 'Lung inflated 2' were recorded at 2 and $4.4\,mm\,H_2O$ equivalent thickness, respectively. The series 'Lung empty 1' and 'Lung empty 2' were recorded at 7.6 and $4.6\,mm\,H_2O$ equivalent thickness, respectively. These values are additionally indicated in Fig. 17. While in Fig. 17 comparison of the different series is difficult, exactly due to differences in sample thickness, the R values in Fig. 18 directly allow for it (see Eq. 12). For measurements done on the symmetric Talbot-Lau GI a general increase of the dark-field and R values can be observed with an increasing auto-correlation length. Simultaneously, an decrease in the slope is seen in series affected by saturation. Most notably it can be seen on the example of the $20\,\mu m$ to $27\,\mu m$ PMMA spheres displaying strong asymptotic behavior as they saturate. The non-saturated measurement series of inflated porcine lungs places itself close but below the $180\,\mu m$ to $212\,\mu m$ PMMA spheres validating the expected behavior in terms of relevant feature size. Additionally, a strong similarity in terms of the overall behavior between the PMMA spheres and the lungs is observed over the entire range of auto-correlations lengths. While non-inflated lungs generally produce lower dark-field signal than their inflated counter parts, it is found that the two series of non-inflated lungs mostly do not agree. Literature values for comparison from Ludwig et al. 2019 are indicated in Fig. 17 & 18 in red[14].
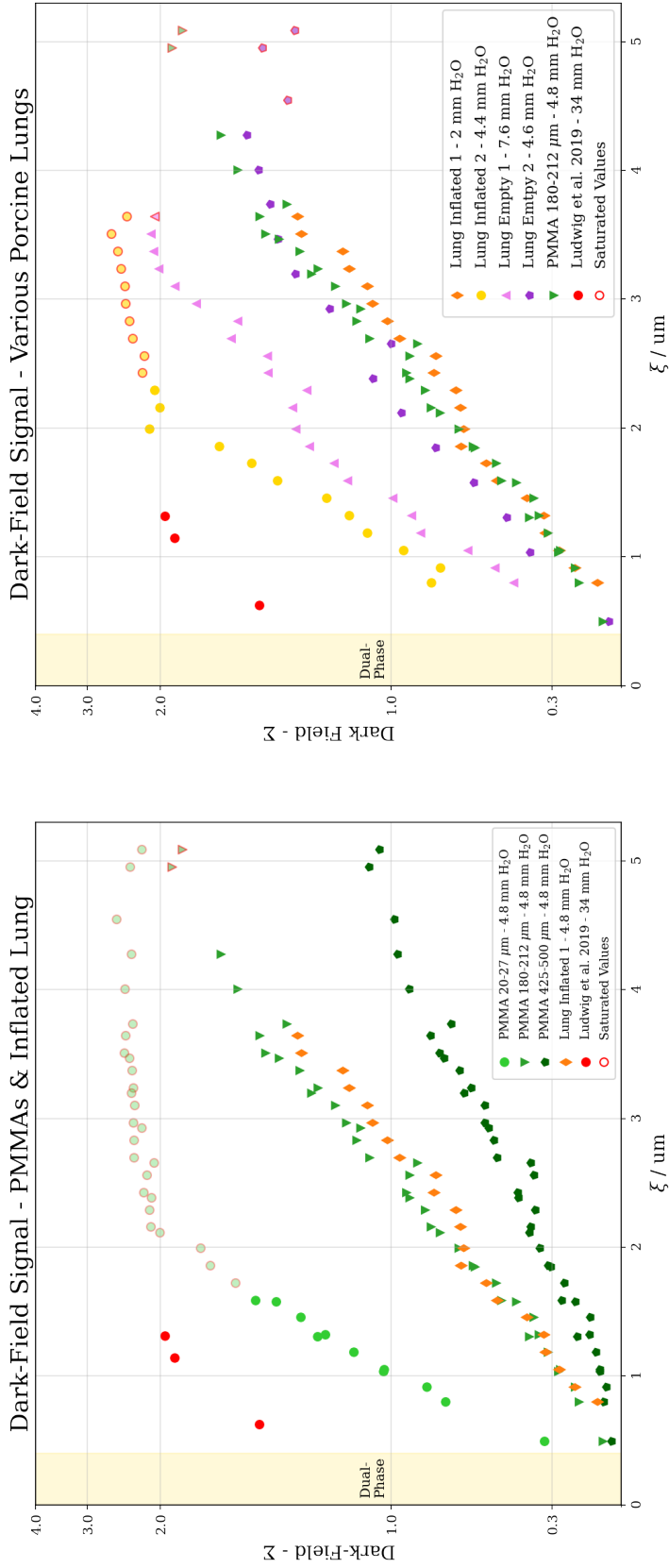
Fig. 17: All dark-field signal measurements plotted against the auto-correlation length at which they were recorded. For the benefit of a better overview, the measurement series were separated. *Left:* All measurements obtained from the PMMA spheres as well as the non-saturating series of inflated porcine lungs. *Right:* All measurements obtained from porcine lung tissue (inflated and not) as well as the series of the 180 μm to 212 μm PMMA spheres for comparison. Beige background marks the range of the dual-phase interferometer.
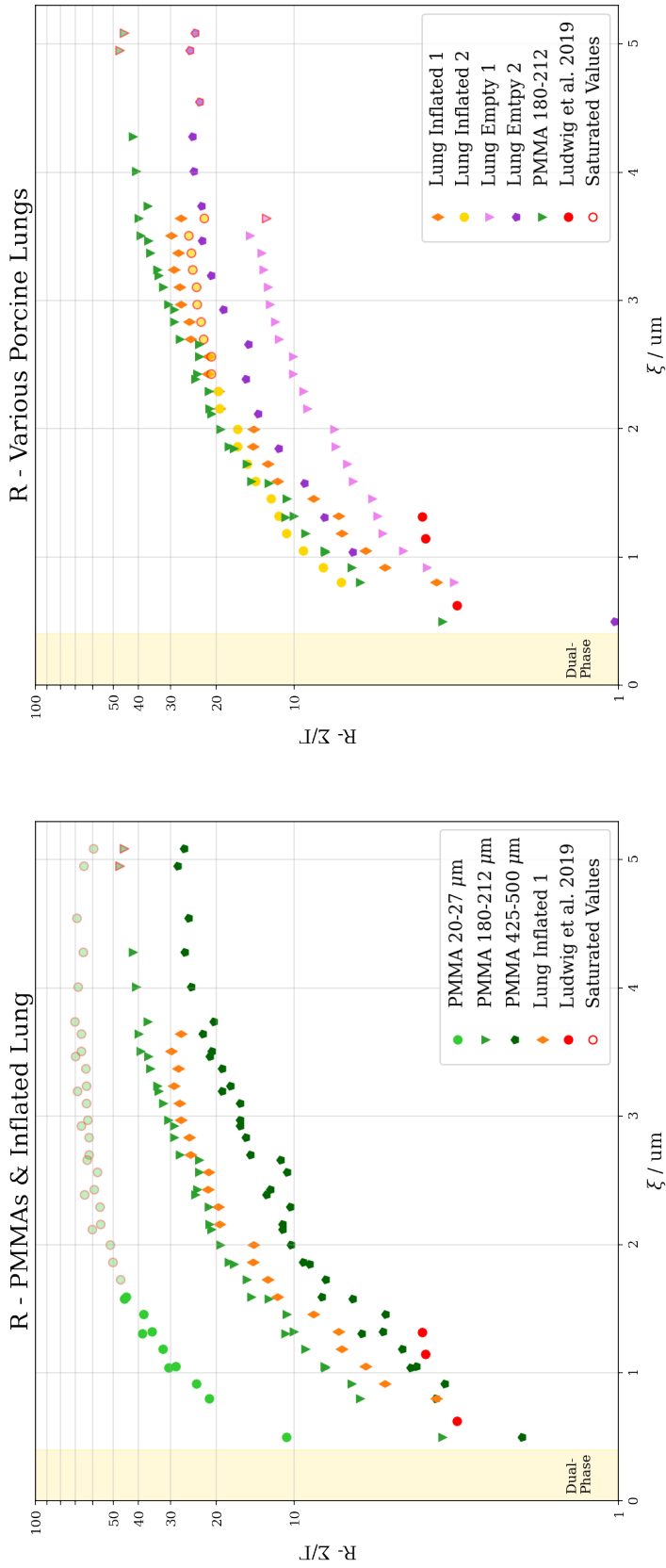
Fig. 18: All R value measurements plotted against the auto-correlation length at which they were recorded. For the benefit of a better overview, the measurement series were separated. *Left:* All measurements obtained from the PMMA spheres as well as the non-saturating series of inflated porcine lungs. *Right:* All measurements obtained from porcine lung tissue (inflated and not) as well as the series of the 180 μm to 212 μm PMMA spheres for comparison. All PMMA sphere measurements were corrected by a factor of 2.84 due to the inverted air/material ration. Beige background marks the range of the dual-phase interferometer.

43

Optimal Auto-Correlation Length for Human Lungs

With a high sensitivity setup towards small angle scattering, the dark-field signal can quickly saturate, as shown here. It is therefore most relevant to be able to estimate the maximal sample thickness yielding non-saturated dark-field signal.

Fig. 19 shows the decay of the visibility V in the sample towards $V_{Noise} = 0.0062$ determined by fitting $V = V_0 \cdot e^{-k\xi} + V_{Noise}$ to the data points of smallest PMMS spheres, the inflated porcine lungs and the non-inflated porcine lungs measured on the symmetric Talbot-Lau GI. In case $V = V_{Noise}$ the dark-field signal is completely saturated.
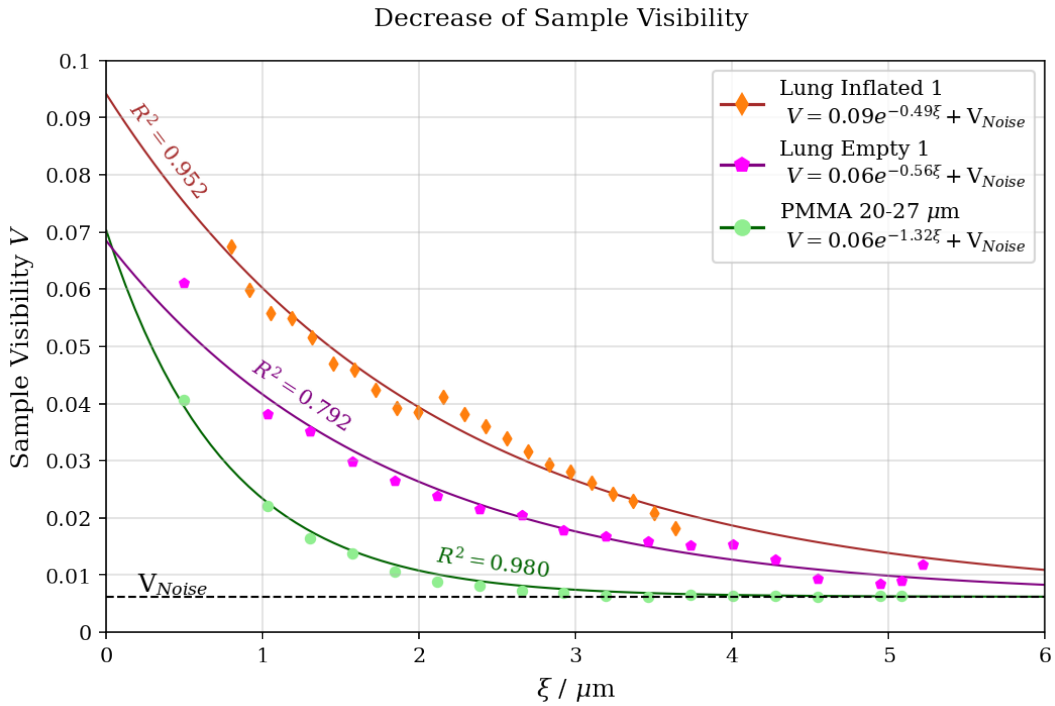
Fig. 19: The visibility of three samples ($20\,\mu m$ to $27\,\mu m$ PMMA spheres, inflated and non-inflated lung tissue) against the auto-correlation length at which they were recorded. $V = V_0 exp(-k\xi) + V_{Noise}$ was fitted towards the three series and returned $V_{Noise} = 0.0062$.

For further computations the measurement series 'Lung Inflated 1' is used which was evaluated at $2\,mm\,H_2O$ thickness equivalent at the lung's apex. The density of the lower lung during inspiration has been shown to be $\rho_L = 0.154\,g/cm^3$[51] The mass attenuation coefficient of lung tissue (LT) at $46\,keV$ has been reported to be $\mu_{LT} = 0.24\,g/cm^2$[52]. Based on the definition of the three contrast channels given in Eq. 9 and the maximal

dark-field signal obtainable before saturation

$$\Sigma_{max} = -\ln\left(\frac{V_{Noise}}{V_0}\right), \tag{17}$$

it follows that

$$\frac{\Sigma_{max}}{R(\xi)} = \Gamma = \ln\left(\frac{A_0}{A_1}\right). \tag{18}$$

By inserting $A_1 = A_0 e^{-\mu_{LT}\rho_L t_{max}}$ and solve for t_{max} we arrive at

$$t_{max} = \frac{\Sigma_{max}}{R(\xi)} \cdot \frac{1}{\mu_{LT}\rho_L}, \tag{19}$$

where t_{max} is the maximal sample thickness before saturation and $R(\xi)$ is the R-value of material in question at the auto-correlation length ξ. For large $R(\xi)$, t_{max} will tend towards t_{Sample} as can be shown by additionally inserting

$$R(\xi) = \frac{\Sigma_{max}}{\Gamma}, \tag{20}$$

into Eq. 19.

Fig. 20 shows the corresponding values of t_{max} for the series 'Lung Inflated 1'. The maximal dark-field signal used was $\Sigma_{max} = 2.095$ based on $V_{Noise} = 0.0062$ and the flat field visibility in the corresponding region of interest. The theoretical shift of $t_{max}(\xi, V_{Noise})$ as reaction to multiple different values for V_{Noise} are indicate by dashed lines, effectively representing lower/higher dose.

The maximal traversed path for X-Rays within lung tissue in a posterior-anterior imaging orientation in humans was estimated to be roughly $t_{max} = 20\,\text{cm}$ based on open accessible human chest CT scans[53] and is indicated in Fig. 20 by the black dashed line. The blue area indicates the range of $\xi = (0, 0.73]\,\text{µm}$ that allows for imaging healthy human lungs in an inflated state without encountering saturation effects. Pathologies only lead to a decrease in dark-field signal and as such operating close to ξ_{max} is reasonable. Minimal

visibility V_{Noise} directly depends on photon counts and as such is proportional to $\sqrt{t_{exp}}$, with t_{exp} being the exposure time and assuming Poisson statistics.
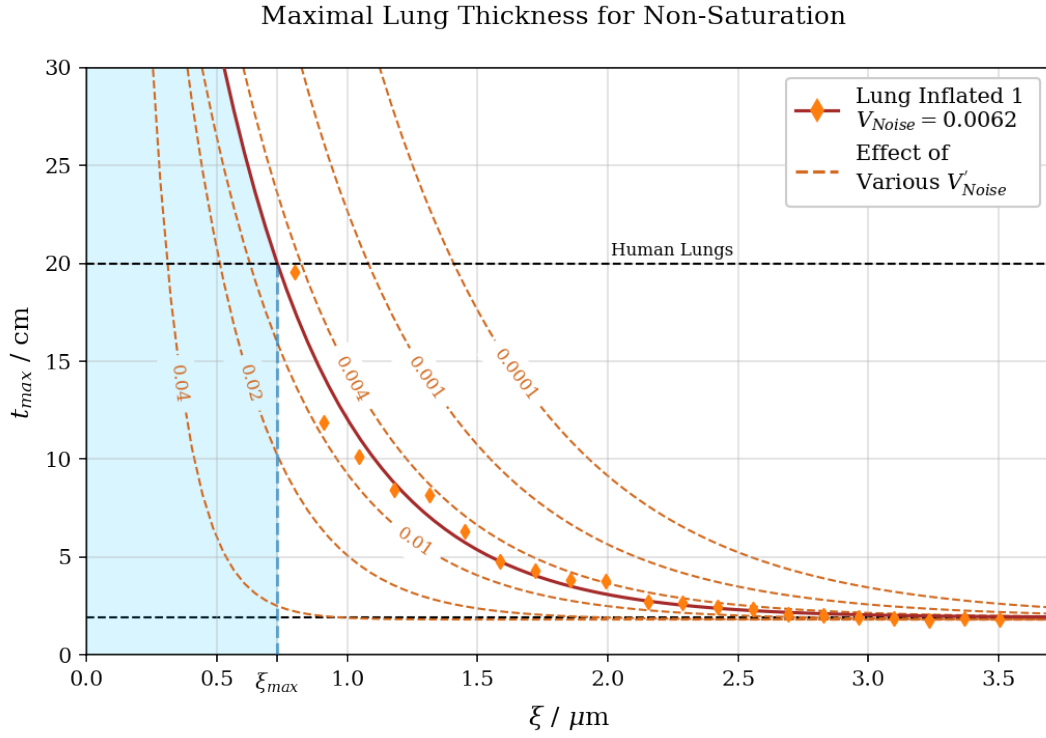
Fig. 20: The maximal lung thickness possible to image at a given auto-correlation length without encountering saturation of the dark-field signal according to Eq. 19. Measurements indicated in orange were taken at $V_{Noise} = 0.0062$. Lines for various different V'_{Noise} are indicated.

Imaging on the Dual-Phase Interferometer
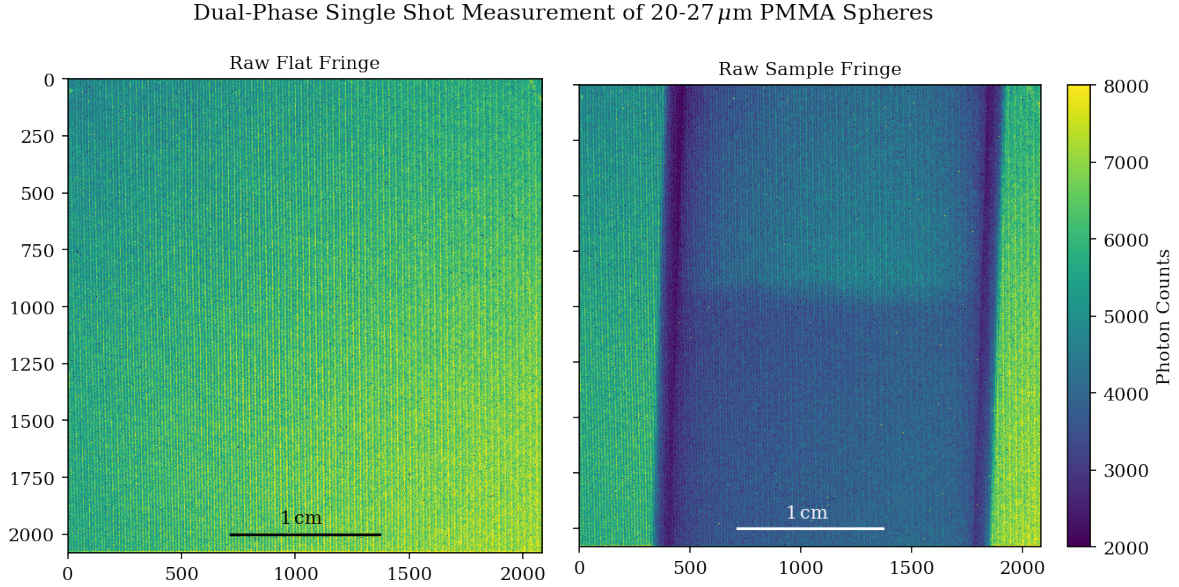
Fig. 21: The raw fringe as generated by the dual-phase interferometer and recorded with a 24 μm CCD camera. *Left:* The flat field fringe. *Right:* The fringe in combination with a vial containing 20 μm to 27 μm PMMA spheres. The flat field visibility was 6 % and the exposure time 20 s.

Fig. 21 shows the complete field of view of the dual-phase interferometer as achieved with the 24 μm CCD camera. On the left the raw flat field image is show while on the right a raw sample scan of a vial containing 20 μm to 27 μm PMMA spheres can be seen. In both cases, the fringe was directly resolved without phase-stepping. These images were taken at the minimal inter-grating distance possible of $d = 4.5$ mm equating to an auto-correlation length of ca. $\xi_{DP} = 0.077$ μm expected to produce a maximal fringe period p_f equal to ca. 400 μm. With a pixel size of 24 μm a minimal fringe period of 96 μm can be resolved reliably, according Nyquist's sampling theorem ($\xi_{DP} = 0.3$ μm). Fig. 22 shows a zoomed-in part of the raw sample scan on top and the line profile along the indicated red line below. Although the fringe is clearly visible in this image, it does not show the expected sinusoidal behavior. Instead, the fringe appears to consist of two frequencies resulting in an alternating beating pattern of minor and major peaks with a period of ca. 405 μm. The alternating beating pattern is clearly visible in the green line profile (Fig. 22 *Bottom*). The blue part of the line profile further shows the effect of the PMMA sphere sample on the fringe. It demonstrates the expected attenuation as well as amplitude dampening due to small angle scattering. All PMMA sphere samples as well as inflated porcine lungs were imaged on the dual-phase setup at inter-grating
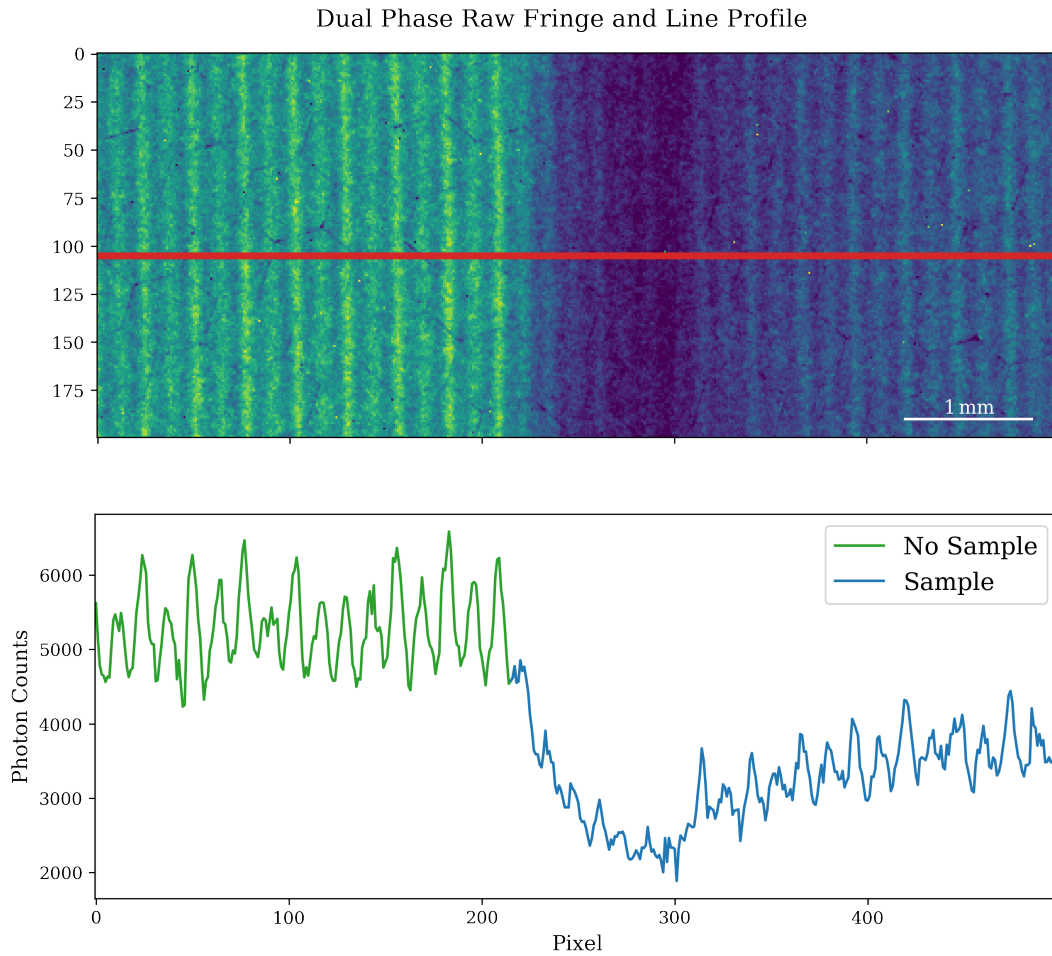
Fig. 22: *Top:* A close up view of the fringe at the edge of the vial containing 20 μm to 27 μm PMMA spheres. *Bottom:* The line profile along the indicated red line. Note how the regularity of the fringe is persistent across the entire line profile marked in red but interaction with the sample attenuates, shifts and blurs the fringe. The unexpected beating effect with major and minor peaks is well seen at the edge to the vial.

distances of $d = 4.5, 7, 12.5$ and 17.5 mm. The same non-sinusoidal fringe behavior was found for all measurements. Flat field visibility was 6%.

As the dual-phase setup can be operated in single-shot mode as well as with phase-stepping the faster single-shot method was chosen. As the fringe no longer adhered to a sinusoidal pattern, an alternative model was required for adequate signal retrieval on

the raw fringe data. It was found that a model consisting of two sine functions

$$I_i(x) = A_0 + C_1 sin(\omega_1 x + \varphi_1) + C_2 sin(\omega_2 x + \varphi_2) \quad \text{with} \quad i = f, s \tag{21}$$

matched the observed fringe well, with $\omega_2 = \omega_1/2$. While linearization for efficient fitting is still possible, obtaining simple formulas for minimal and maximal values of the resulting fringe $I_i(x)$ for visibility calculations, proved challenging. It was therefore decided to follow an alternative approach for signal evaluation.

Blurring of the flat field interference pattern I_f by small angle scattering can be understood as a convolution of the fringe with a Gaussian function. By convolution of the model given in (8) with said Gaussian

$$g(x, \sigma) = \frac{1}{\sqrt{2\pi\sigma^2}} e^{-\frac{(x-\mu)^2}{2\sigma^2}}, \tag{22}$$

and using (15) as well as the definition of the dark-field signal Σ given in (9), it can be shown that

$$\Sigma \propto \sigma^2. \tag{23}$$

Based on this, the idea was to fit (21) to the flat field fringe in a first step and obtain the parameters A_0, C_1 and C_2 which are not affected by the blurring. In a second step, fitting

$$I(x, \sigma)_s = I_i(x) * g(x, \sigma) \tag{24}$$

would then return σ allowing for quantification of the dark-field signal. It is directly possible to introduce parameters accounting for absorption and phase-shift as well and returning all three contrast channels simultaneously, as a result of the fit. The implementation of this convolutional approach to signal quantification in dual-phase GI proved cumbersome, calling for a more efficient and direct way to analyze the images.

The final solution which was used for signal retrieval based on a single image is described in the following and is based on Fourier analysis. Using a single line-profile of the image over a few pixel perpendicular to the fringe's direction (as shown in Fig. 22 *bottom*)

as signal function $s(x)$, it is readily possible to calculate the Fourier spectrum of said signal. This can be done for the flat as well as for sample signal. The complex Fourier spectrum

$$F_i(\omega) = (\mathcal{F}s_i)(\omega) = \frac{1}{\sqrt{2\pi}} \int_{-\infty}^{\infty} s_i(x) \mathrm{e}^{-\mathrm{i}\omega x} \, \mathrm{d}x \quad \text{with} \quad i = f, s \tag{25}$$

provides all information necessary to calculate the absorption, phase as well as dark-field signal. The three contrast channels can be retrieved by

$$\Gamma = -\ln\left(\frac{F_s(0)}{F_f(0)}\right), \quad \Sigma = -\ln\left(\frac{F_s(\omega_{fringe})/F_s(0)}{F_f(\omega_{fringe})/F_f(0)}\right)$$

$$\Delta\varphi = \tan^{-1}\left(\frac{\mathrm{Im}(F_s(\omega_{fringe}))}{\mathrm{Re}(F_s(\omega_{fringe}))}\right) - \tan^{-1}\left(\frac{\mathrm{Im}(F_f(\omega_{fringe}))}{\mathrm{Re}(F_f(\omega_{fringe}))}\right). \tag{26}$$

This was found to be the most practical and most reliable method. Fig. 23 shows all three retrieved contrast channels as well as the R-image resulting from the combination of dark-field and absorption for $20\,\mu\mathrm{m}$ to $27\,\mu\mathrm{m}$ PMMA spheres at $\xi = 0.077\,\mu\mathrm{m}$. The corresponding measurements for inflated porcine lungs are shown in Fig. 24. The absorption and phase images look as expected: In Fig. 23 absorption clearly indicates the presence of spheres in the vial and phase highlights the edges of the vial clearly. In Fig. 24, absorption shows the imaged part of the inflated lungs including some airway-structures. The phase image of the porcine lungs segment is mostly noise and artifacts as no clear, sharp edges are present in the lung. Although the presence of dark-field and R signal agrees with the location of the sample as indicated by the absorption image, the images show a gradient of the mean signal strength from left to right. While present in either case (PMMA & lungs) it is more dominantly visible in case of the porcine lungs.

Fig. 25 shows the R-values of measurements done on the dual-phase interferometer of all three PMMA spheres investigated as well as the inflated porcine lungs. While the signal of all PMMA spheres is strongly decreasing with an increasing auto-correlation length the signal of the inflated porcine lungs increases slightly. This is in clear contrast to any results found on a classical TLGI, as spheres and lungs do not agree with each other in terms of their trends. Additionally, the $425\,\mu\mathrm{m}$ to $500\,\mu\mathrm{m}$ and $180\,\mu\mathrm{m}$ to $212\,\mu\mathrm{m}$ spheres are hardly distinguishable from each other based on the dual-phase data, while the $20\,\mu\mathrm{m}$ to $27\,\mu\mathrm{m}$ spheres still produce a clearly higher dark-field signal.

Dual-Phase Measurement of 20-27 μm PMMA Spheres
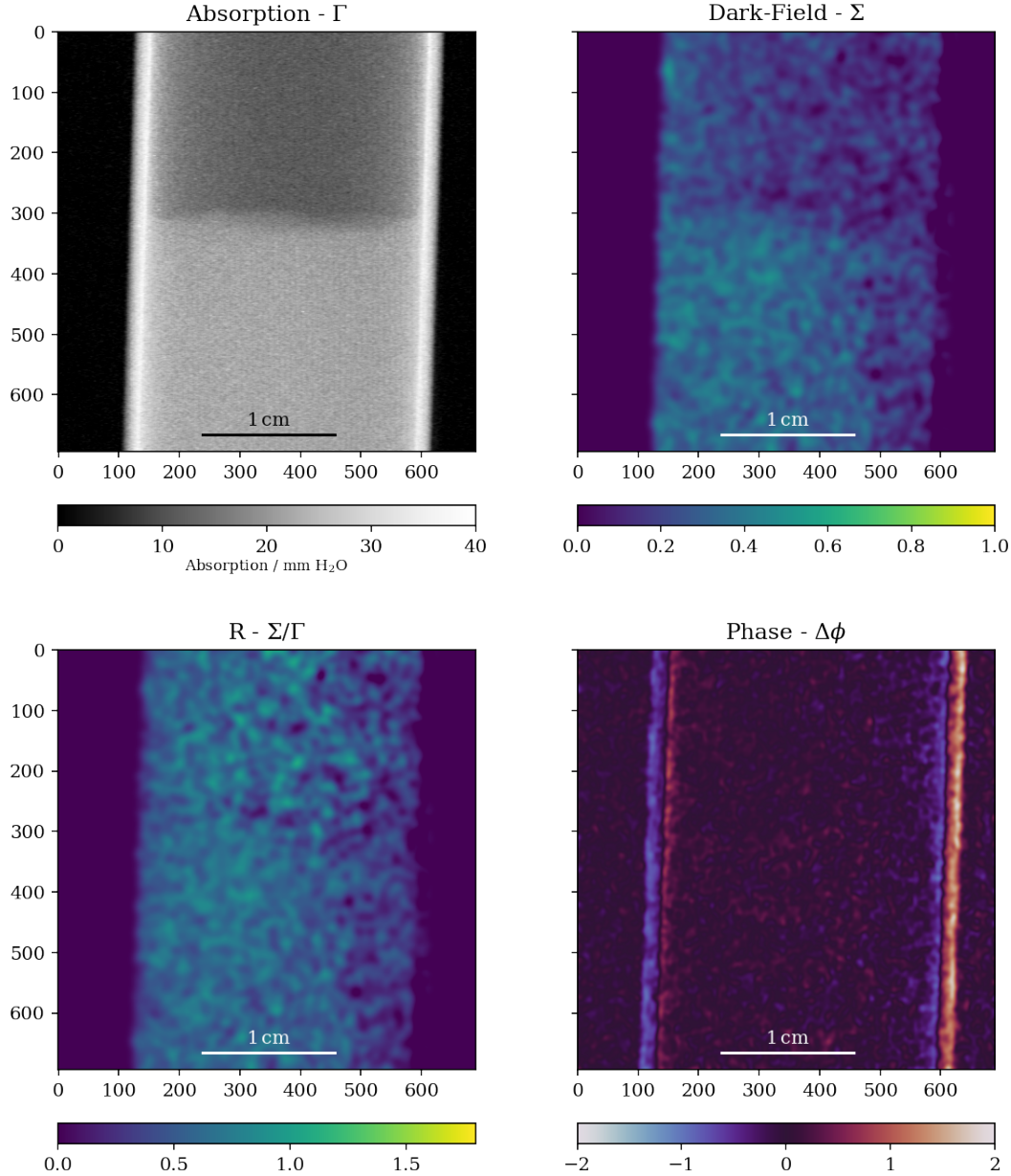
Fig. 23: The results of Fourier Analysis based signal retrieval from a single-shot measurement on the dual-phase interferometer of 20 μm to 27 μm PMMA spheres at $\xi = 0.077$ μm. *Clockwise from Top Left:* The absorption, the dark-field, the phase and the resulting R image. PMMA spheres were imaged with 70 kVp at 200 μA with an exposure time of 20 s. Note how the area of low attenuation above the spheres (empty glass vial) lights up in the R image. This can be attributed to a paper sticker on the outside of the vial or beam hardening effects.

Dual-Phase Measurement of Inflated Porcine Lungs
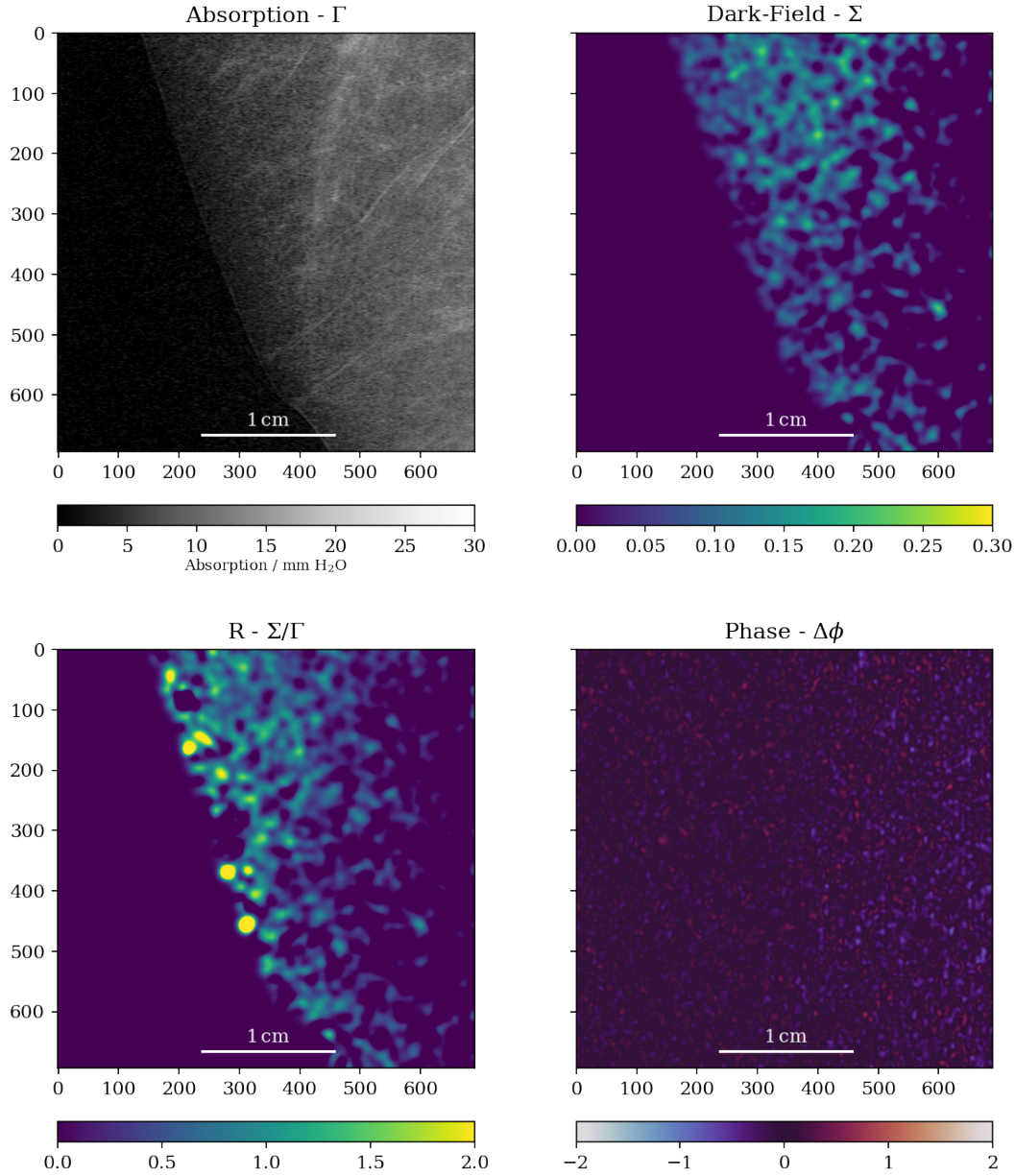
Fig. 24: The results of Fourier Analysis based signal retrieval from a single-shot measurement on the dual-phase interferometer of inflated porcine lungs at $\xi = 0.077\,\mu m$. *Clockwise from Top Left:* The absorption, the dark-field, the phase and the resulting R image. Inflated porcine lungs were imaged with $70\,kVp$ at $200\,\mu A$ with an exposure time of $20\,s$. Notably, no saturation was observed on the dual-phase system but still a gradient in the R image from the edge towards the center of the lungs is observed.
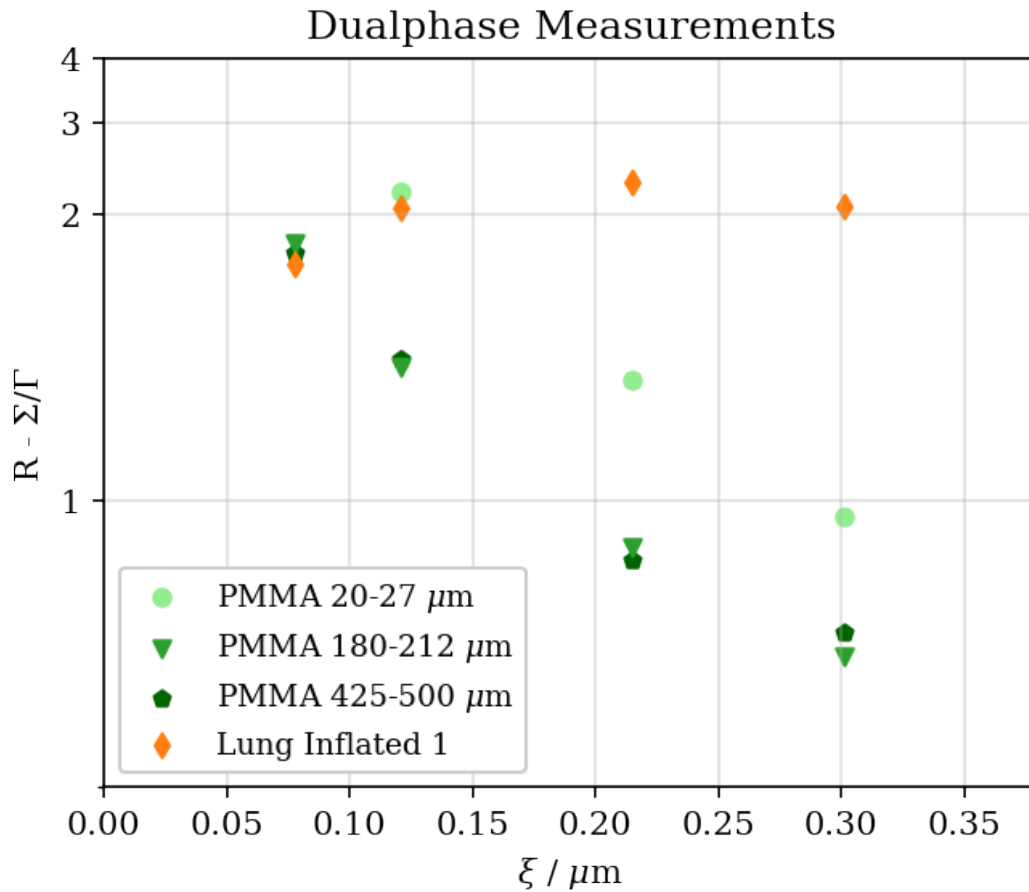
Fig. 25: The results obtained from the dual-phase interferometer for PMMA spheres and inflated porcine lungs. The retrieved values not only defy expectations in terms of trends but as well in relative magnitude as the inflated lung's signal remains high while the PMMA sphere's signal drops rapidly.

Discussion

Porcine Lungs as a Substitute

Based on the most common farm animals used today which are slaughtered on a regular basis, pigs are the closest to human in terms of size and structure. While porcine lungs show slightly different anatomical features in terms of number and placement of lung lobes, compared to human lungs, they are generally a good stand-in and have been used extensively in translational medicine over the past decades[54]. While measuring a representative average alveolar size is in itself a caveat rich undertaking[55], additional shrinking effects due to histological sample processing and the native elasticity of lung tissue complicate qualitative analysis even further.[18,56]. Generally, alveolar size in pig and humans is considered comparable while porcine lungs might show slightly smaller features[57]. The study supports these findings as the thickness corrected dark-field signal R of inflated porcine lungs is found to be slightly lower than for PMMA Spheres with a size range of $180\,\mu m$ to $212\,\mu m$ (see Fig. 18).

The means to obtain, handle, inflate and image human-sized lungs have been established in this study. While inflating lungs by applying a positive pressure works extremely well, we deemed it important to replicate the manner of ventilation as found in the human and porcine body. Establishing a negative pressure surrounding the lungs came with a few additional challenges but proved valuable as the container simultaneously acted as a stable sample holder allowing for almost interaction-free imaging inspired by [48]. Compared to direct pressurization of the lungs, inflation by vacuum requires various additional seals and tight connections, however, no complete seal was required and in fact was not achieved as the lungs obtained from the slaughter house displayed minor (and sometimes major) injuries and cuts. A valve connecting the under-pressurized volume to the surrounding allowed to regulate the pressure difference readily to the desired level, while keeping the vacuum pump running at all times. As the lungs were contained in a closed container with almost no air-circulation their surface did not dry-up, keeping them humid also over longer imaging sessions. While -30 mbar was the maintained idle pressure representing normal *in vivo* conditions[18], the range of pressures during inspiration *in vivo* is quite large, ranging from -1 to -100 mbar, mostly depending on the level of stress and the overall health of the respiratory system. Furthermore, it was not possible to judge the level of inflation directly but proper recruitment of alveoli was assumed after letting the lungs settle for 1 hour at -30 mbar. While this is a limitation of this study, direct verification of the inflation is not possible without damaging the lungs and as such affecting the pressure/inflation levels, rendering the task void. Faster and likely increased recruitment of collapsed alveoli could be achieved by periodically cycling through phases of inspiration and expiration, effectively simulating a breathing cycle, with increased pressures before imaging, as it is done in humans

suffering from respiratory distress syndrome[58]. This helps redistributing the surfactant faster in collapsed airways leading to faster and more complete inflation but also poses the risk of mechanical ventilation-induced damage.

While the presented system here reliably inflates the lungs and maintains a constant pressure comparable to *in vivo* conditions, it lacks distinct features present in the human body. Most notably the lack of a volume-confining structure acting against the lung's expansion similar to the human rib-cage and its musculature as well as the lack of the heart and any circulatory effects. Biederer et al. showed the construction of a thorax phantom based on porcine organs, capable of displaying a working breathing cycle as well as perfusion[48]. For future investigations towards clinical applicability a similar system might be required. Whether it is easier to construct such a thorax-phantom or to work with porcine bodies remains to be seen.

All in all, porcine lungs provide a valid, readily obtainable model for pre-clinical lung research directly comparable to human lungs. Inflation can readily be achieved by positive as well as negative pressures as has been shown here. Our results further confirm the expected feature size slightly above 200 µm by comparison to PMMA spheres on the basis of their thickness corrected dark-field signal. Future investigations might require a more extensive preparative approach, representing the *in vivo* conditions more closely.

The Dark-Field Signal of Porcine Lungs

It has repeatedly been shown in literature as well as in this work, that lungs are suitable for dark-field imaging due to their inherent porous structure[12–14,59,60]. Still, no study investigated as to which features of the lung's anatomy actually generates the detected dark-field signal. While it would be erroneous to assume that only one distinct structural aspect causes small angle scattering, it is most relevant to narrow down the range of contributing feature-sizes with respect to signal interpretation. Only an *ab initio* approach could explain this in full detail allowing to control each aspect of the sample and beam interaction, however, for complex structures this a most challenging endeavor. By imaging samples with a well-defined structure, as was done here, it is possible to narrow down the responsible feature size by comparison. PMMA spheres of 20 µm to 27 µm lead to the strongest dark-field signal, quickly saturating it as well. Similarly PMMA spheres of 180 µm to 212 µm and 425 µm to 500 µm generate proportionally less signal. It has been shown here, that the the R values of inflated porcine lungs can be found close but below the 180 µm to 212 µm but clearly above the 425 µm to 500 µm PMMA spheres suggesting a feature size of above 200 µm. This agrees nicely with reported values of alveolar diameters in literature[18] of ca. 250 µm supporting the assumption that it actually is the terminal alveolar structure which responsible for the dark-field signal. Note that for comparison of lung structures with PMMA spheres a correction of the R-value by a factor 2.84 was necessary based on the inverted matter/air ratio, assuming optimal

sphere packing. While alveolar shape is clearly distinct from spheres and often described as 'polygonal', it likely is a valid assumption that PMMA spheres arrange themselves close to optimal sphere packing geometry. As such, correction of the different absorption behaviors on this basis, allows for direct comparison of the PMMA sphere's and the lung's R values. The overall similarity in behavior of the dark field signal between the lungs and the PMMA spheres is an additional benefit. As such, PMMA spheres are a suitable stand-in for lung samples. As various sized spheres are obtainable, it should be possible to find a size of PMMA spheres that directly agrees with measurements taken from lungs - inflated, non-inflated, healthy as well as pathological (e.g emphysematous). The ability to mix different sizes, creating anisotropic samples provides for even more possibilities. Finally, with the prospects of a future clinical imaging system, PMMA spheres likely lend themselves for the design of a calibration and validation phantom.

Furthermore, our data shows that non-inflated lungs generally scatter less than inflated ones. Without any pressure applied to the airways, they collapse leading to significant loss of air-tissues interfaces which are essential for the generation of the dark-field signal. Conspicuously, the two series of non-inflated lungs don't agree as well as the two series of inflated lungs (see Fig. 18). This is not too surprising. Non-inflated lung tissue was recorded in parallel to the inflated ones in form of a cut-out cube of lung tissue. No attention was paid at the time of preparation that the two tissue samples originate at the same location of the lungs and both have been frozen for some time before imaging. During the image process (which took up to 9 hours) the samples quickly thawed, leading to a loss of liquid, as is commonly experienced with frozen meat. It is therefore suspected that also the micro-structures of the tissue were increasingly subjected to an excess of liquid, which likely influenced the recorded signal. Nevertheless, we do report detectable dark-field signal also for non-inflated lungs. This is most relevant as in a future clinical scenario, not all patients will be capable of breath holding nor will they be necessarily healthy. As such, depending on the state of inspiration the level of dark-field signal changes.

This study's results further demonstrates the behavior of the dark-field signal of inflated porcine lungs over a wide range of auto-correlation lengths, filling in gaps of a previously sparse data set. Previous to this work, well defined dark-field signal for inflated lungs was reported by Ludwig et al. in 2019 at three distinct auto-correlation lengths (see Fig. 17 & 18), measured in a lung-heart phantom on three different Talbot-Lau GI[14]. The auto-correlation lengths presented were $\xi_{L19} = 0.62, 1.14, 1.31 \, \mu m$ The range of auto-correlation lengths presented in this thesis reached from $0.8 \, \mu m$ to $3.64 \, \mu m$ with an average sample density of $7.8 \, \mu m^{-1}$ clearly exceeding previously reported results. While the lungs clearly produced signal at all sampled auto-correlation lengths, the upper range sampled, quickly lead to saturation effects which have not been discussed before with regard to lung imaging. This demonstrates that maximized sensitivity towards small angle scattering can quickly result in destruction of the signals information content as the interference pattern is no longer distinguishable from pure noise. Obtaining unsaturated

signal even for auto-correlation lengths above $2\,\mu m$ is feasible by reducing the sample's thickness. Looking at the published values from Ludwig et al. in Fig. 17, it is clear that these measurements were taken at a much higher sample thickness - estimated at $t_{L19} = 20\,cm$ lung thickness based on the absorption image - explaining the higher dark-field values. In the R-plot (see Fig. 18) the lowest value corresponds nicely to the values presented here, however, at $\xi_{L19} = 1.14$ and $1.31\,\mu m$ the literature values are significantly lower. With a pure dark-field signal of $\Sigma_{L19} = 1.94$ and 1.98 these values likely suffer from saturation, leading to an understatement of the true dark-field signal. Comparing this to the maximal lung thickness given in Fig. 20, reinforces this suspicion, as with a lung sample of $20\,cm$ saturation occurs already at $\xi = 0.73\,\mu m$ - assuming a comparable V_{noise} .

In 2018, Vignero et al. [61] estimated that if human lungs had the same structure as murine lungs, $2\,cm$ sample thickness would suffice to saturated the signal based on a TLGI with $\xi \approx 1\,\mu m$. However, they concluded that due to a factor of ca. 5 times larger alveolar structures in humans compared to murine lungs, sensible dark-field signal should be retrievable. They estimated the dark-field signal for humans lungs as a function of the sample thickness between 0 and 20 cm. For the equivalent thickness of $2\,mm\,H_2O$, they arrive at $\Sigma = 0.16$. Compared to the measured results presented here $\Sigma(1\,\mu m) \approx 0.3$ these results seem to be underestimated. However, as our measurements were placed specifically to avoid saturation effects, the apical location of the measurement could have lead to a slightly higher result than in a central location. This due to the fact, that the alveolar density is higher in the lower lungs. On the other hand it has been suggested that these local variations of alveolar density can be neglected by "factoring in the effects of alveolar compression due to the pleural pressure gradient at the base of the lung in vivo and at functional residual capacity"[62], concluding that the estimate from Vignero et al. was indeed too low.

Finally, it is reported here, that on the basis of our measurement a maximal sample thickness can be estimated for a given auto-correlation length. Assuming a maximal lung thickness in an anterior-posterior (AP) orientation of $20\,cm$, a maximal auto-correlation length of $\xi_{max} = 0.73\,\mu m$ results, as indicated in Fig. 20. For practical applications, operating at the maximal level of detectable visibility loss is not recommended as saturation effects already influence the results before reaching the threshold. As a next step, the limitations of clinical acceptable dose should be defined on the basis of which V_{Noise} can either be estimated or measured. In combination with the data shown in Fig. 20, it is possible to estimate an auto-correlation length capable of handling human sized lungs without exposing the patient to higher dose levels than conventional radiography does under current clinical standards.

The data presented here has some limitations. First, imaging of inflated porcine lungs in a vacuum chamber is efficient and relatively easy to setup in a lab-environment, but it does not represent the *in vivo* conditions directly and it is hard to judge the inflation

levels of the lungs. An entire porcine carcass might provide a more complete picture but is simultaneously exponentially more effort to obtain, handle and accommodate. In the current state of the setups used here, it would certainly exceed the possibilities of the facility. Secondly, porcine lungs are close to, but not identical with human lungs. Slight differences in terms of macro- as well as micro-structure are present. A validation study using an excised human lung could further validate the findings shown here and allow to push towards a more complex phantom. Whether further investigations should be porcine based or human based has to be considered carefully.

In summary, parallel imaging of inflated porcine lungs and PMMA spheres of comparable size allowed to reinforce the hypothesis that indeed the alveoli and alveolar ducts are responsible for the dark-field signal. As such, changes observed with the progression of pathological changes in the dark-field signal of the lung (as reported here [12, 60]) can effectively be attributed to a loss of alveolar structures rather than the general loss in lung tissue. Dark-field and R values over a wide range of auto-correlation lengths are provided for inflated and non-inflated lungs for a first time and on their basis a maximal auto-correlation length, capable of handling human sized lungs in an AP orientations, is estimated. Effects of different dose levels on the optimal auto-correlation length are indicated.

Signal Saturation - The Drawback of Maximizing Dark-Field Sensitivity

Signal saturation in dark-field imaging is an expected effect. Once the noise level surpass the visibility of the phase stepping curve, no reasonable retrieval of the dark-field signal is possible. As dark-field imaging relies on the visibility loss caused by the sample due to small angle scattering, the imaging setup has to be designed in a way, such that it is capable of handling the intended sample without saturation. It is therefore not a general advantage to maximize the system's sensitivity. While technically true, that saturation could be reduced by an increased exposure time, this is mostly impractical as

$$S_{Sat} \propto \frac{1}{\sqrt{t_{exp}}}, \tag{27}$$

where t_{exp} is exposure time and assuming constant photon flux.

In 2014, Strobel et al. reported that the dark-field signal of hard spheres stabilizes at $\Sigma = \sigma t$ once the threshold of $\xi = d$ is exceeded, where σ is the scattering cross section of the system, t the sample thickness and d the diameter of the spheres under investigation[63]. This stabilizing effect, however, is not observable in our measurements, as

the maximal auto-correlation length ξ reached was $5.2\,\mu m$, coming short of the smallest spheres diameter by a factor of 5. In our case, the asymptotic tendency, best seen in the $20\,\mu m$ to $27\,\mu m$ PMMA spheres, towards a constant dark-field signal can clearly be attributed towards signal saturation. Making the level of saturation accessible by defining a saturation score (Eq.16 & Fig.16), possible to quantify for each pixel, further confirms this notion. While in this study an empirical threshold for S_{sat} of 0.78 was used to classify individual measurements regarding their saturation, a more in-depth investigation would be necessary to identify the optimal threshold. Furthermore, it needs to be added that the assumption of Poisson statistics only holds for photon-counting detectors such as the one used on the inverse and the symmetric TLGI. CCD cameras, in context of this work only used in combination with the dual-phase interferometer, do not only display noise following Poisson's statistics (Shot noise) but additionally higher levels of dark noise and read noise are present. However, in this work, saturation was no problem while working on the dual-phase setup as it was only possible to work at rather small auto-correlation lengths, therefore being less susceptible to visibility loss and saturation.

Inspired by the correction of dark noise in case of CCD cameras

$$\Gamma = -\ln\left(\frac{I_s - I_{dark}}{I_f - I_{dark}}\right),\tag{28}$$

a correction of the dark-field signal could be used employing V_{Noise}

$$\Sigma = -\ln\left(\frac{V_s - V_{Noise}}{V_f - V_{Noise}}\right).\tag{29}$$

By correcting dark-field values according to Eq. 29, no plateauing effect should be observed as seen in Fig. 17 & 18. Instead, the dark-field signal would increase further towards infinity corresponding to infinite visibility loss. For future evaluations of the dark-field signal, this should be considered as a viable option to improve the data quality.

A Dual-Phase Interferometer for Lung Imaging

This study tried to demonstrate the capability of a dual-phase interferometer to image porcine lungs and reference samples. While the fringe does not demonstrate a sinusoidal behavior, as was expected, operation in single shot mode was still possible by employing

Fourier analysis for signal retrieval. The method used for signal retrieval up to this point was based on linearly fitting a sine function to the obtained fringe/phase-stepping curve (see Eq. 8). Attempts to retrieve the signal based on a convolutional model, while theoretical feasible, proved cumbersome and inefficient in its implementation due to the repeated need of curve fitting. Evaluation based on Fourier analysis not only proved to be simpler but exceedingly more efficient highlighting its advantages. The underlying reason for the non-sinusoidal wavefront can only be suspected, however, the following aspects likely contributed to it. For one, we are not working with a monochromatic beam, which certainly will introduce artifacts to interference pattern. It is reminded here, that the design energy was 30 keV while the used CCD works best at 17 keV. Additionally, the setup's cone beam geometry in combination with an offset of the detector from the central beam axis will affect the effective duty cycle of the gratings subsequently affecting the interference pattern. Additionally, it was realized, that the grating-stage did not provide a optimal perpendicularity of G_1 to G_2, leading to a slight shift in fringe period p_f across the field of view. The observed gradient in the dark-field and R images in Fig. 23 & 24 might be partly attributable to this local change in auto-correlation length as well as the cone beam geometry. It is not clear at this stage what the true reason for the displayed behavior is, however, likely it is a combination of the factors mentioned here.

Nevertheless, PMMA spheres as well as inflated porcine lungs were imaged on the dual-phase interferometer and evaluated as mentioned above.

It was found that various sizes of PMMA spheres (20 to 27, 180 to 212 and 425 to 500 µm) as well as porcine lung generate a detectable visibility loss with $\xi \in [0.077, 0.301]$ µm on our dual-phase setup. However, contrary to all our expectations, the dark-field signal strictly decreases with an increasing auto-correlation length for all PMMA samples. The magnitude of the R values is also higher for all measured samples, than what was expected based on the measurements performed on the TLGIs. In light of the trend-wise similarities of PMMA spheres and all lung samples on the TLGIs, further similarities were expected at lower auto-correlation lengths as well. However, this expectation was not confirmed as can clearly be seen in Fig. 25. Furthermore, the apparent gradient observed in the dark-field and R images further feed the suspicion that there is an inherent problem with the measurements taken on the dual-phase interferometer. While the recorded values of the dual-phase interferometer are clearly not trustworthy and a rework of the setups configuration might already improve the results, the following paragraphs will try to outline some possible effects contributing to the observed values here.

Beam hardening effects occur when working with poly-chromatic sources and cause visibility reduction even in the absence of small angle scattering. While changing the position of the sample along the beam axis in a Talbot-Lau GI affects the magnifications, it does not affect the overall geometry of the interferometer. As such, beam hardening

effects are constant in all measurements performed with the same sample on the same TLGI. In case of the dual-phase interferometer though, a change of the inter-grating distance (aka. the auto-correlation length) effectively changes the geometry of the setup and as such its spectral acceptance and with it the influence of beam hardening. In 2020, Pandeshwar et al. developed the theoretical frame work to account for these beam hardening effects in dual-phase interferometers and demonstrated how such effects could be corrected[46]. In their publication, they show results from two micro-sphere powders with 0.26 and 1.7 µm diameter, behaving drastically different over the same range of auto-correlation lengths, confirming and correcting their results based on their frame work. These results demonstrate, that even a small change in feature size, can have major impacts on the behavior of the dark-field as a function of the auto-correlation length. Comparing our measurement to their uncorrected ones - even though the feature size is wildly different - shows that a decrease in dark-field signal with increasing ξ might be explained to some degree by their model as an effect of beam hardening due to the spectral acceptance of the interferometer. It is therefore suggested, that simultaneously to improve the setups configuration, an improvement in data processing is required, eventually correcting for beam hardening effects due to the spectral acceptance of the interferometer.

For all samples (PMMA & lung) it was ensured that the region of interest, placed in the image, was located at the same place, ensuring constant sample thickness. While this ensures comparability of the dual-phase data points in Fig. 25, the sample itself will cause additional beam hardening effects.

While a gradient is found in the dark-field as well as in the R images of PMMA spheres as well porcine lungs, it is more dominant in case of the lungs and clearly coincides with an increase in sample thickness. The change in sample thickness will cause additional beam hardening. The thickness can be judged from the absorption image in Fig. 24. Beam hardening causes an underestimation of the visibility, inversely leading to an overestimation of the dark-field signal. It is therefore suspected that while an inherent gradient is already present due to improper alignment of the two gratings, it is additionally reinforced in the porcine lung images due to beam hardening. Beam hardening due to the sample cannot be eliminated while working with poly-chromatic sources, it can be mitigated by filtering the beam before the sample.

Lastly, operation of the setup with an exposure time of 20 s resulting in 40mAs might not provide sufficient statistics in combination with the beam hardening as proportionally a larger amount of the detected counts result from energies above 30 keV. This will give a wrong estimation of the visibility and therefore affect the dark-field signal. Longer exposure times might therefore improve the measurements. Due to a lack of time it was sadly not possible to investigated the outlined improvements here to achieve more promising results from dual-phase interferometer.

The possibility of using a dual-phase interferometer for lung imaging in humans is intriguing for several reasons. Without the need of any absorption gratings after the patient (G_2-less), a dose reduction of up to 50% can be achieved compared to a conventional Talbot-Lau grating interferometer, benefitting the patient as well as the applicability of the method in a clinical setting. The lack of G_2 further decreases the cost of the setup drastically. In a conventional Talbot-Lau GI G_2 needs to cover the whole width of the human thorax to allow for proper imaging. As this is currently only feasible for a small and wide field of view (FOV) by combining multiple gratings, vertical scanning is required to image an entire human sized thorax[12,13]. As no analyzer grating is needed on a dual-phase setup at all, this significantly lowers its costs. Furthermore, the method still allows for retrieving all three contrast channels (Γ, $\Delta\phi$ and Σ). The challenge will be to design a dual-phase interferometer generating a fringe large enough that allows working with commercially available, large-FOV detectors. The flexibility of the dual-phase setup in terms of auto-correlation length adds an additional benefit to the system. While both emphysema and fibrosis lead to a general loss in the dark-field signal due to a loss of tissue-air interfaces, it is not possible to distinguish between the two directly based on a single measurement. Taphorn et al. demonstrated on a Talbot-Lau setup, the advantages of dual-energy grating interferometry using a spectral detector, allowing for differentiation between destruction and densification of lung tissue[15]. So far, investigations of dark-field imaging mostly neglect the fact that quantitative information of the scattering structure can be obtained via the specific length scale sensitivity defined by the auto-correlation length of a given setup. Therefore, a dual-phase interferometer could be employed to differentiate between destruction and densification of lung tissue by employing multiple auto-correlation lengths, analogously to Taphorn et al. This is a clear advantage over a classical TLGI, where a change of the auto-correlation length in a clinical setting is most impractical. However, as can be seen from the results presented here in a preliminary manner, detailed investigations on how to overcome spectral and beam hardening effects are required before a conclusive interpretation of these results can be provided. Luckily, one effect not further complicating matters, is signal saturation, which was not observed in any of the dual-phase measurements, as the fringe was always clearly visible.

In conclusion, it was not possible to demonstrate that lungs provide sufficient dark-field signal to be detected on a dual-phase interferometer. This due to suspected spectral and beam hardening effects overshadowing the true dark-field signal. Careful consideration and eventual correction of these effects are required to provide quantitative and comparable results for future investigations. Different methods for signal retrieval were experimented with as the fringe did not adhere to a simple sinusoidal pattern. It was concluded that Fourier analysis is the most reliable and efficient way to do so, allowing for retrieval without an underlying model for the interference pattern. The advantages of a dual-phase interferometer over a classical TLGI are manifold with respect to clinical applications - higher dose effectiveness, lower costs and the hypothesized possibility to

differentiate between different pathologies being the key ones - but at this stage further investigation towards the understanding of the basic dynamics at play in a dual-phase interferometer are required before its applicability for clinical purposes can be judged.

Conclusion

The means to inflate and image porcine lungs in a repeatable manner were established. Inflation by surrounding vacuum, while slightly more complicated and effort-rich, provides reliable results and reproduces the conditions present *in vivo* to a reasonable degree. Based on the symmetric Talbot-Lau grating interferometer, porcine lungs (inflated and non-inflated) were measured at a wide range of auto-correlation lengths characterizing their behavior. Reference samples in form of PMMA spheres with different diameters were measured in parallel. It was found that PMMA spheres are a viable option to simulate healthy as well as pathological lungs, depending on their diameter and might lend themselves for the design of a future lung phantom. Furthermore, these measurements allowed to narrow down the dominant feature size contributing to the dark-field signal of lungs to slightly above $200\,\mu m$. A maximal auto-correlation length, capable of handling human lungs in an AP orientation was estimated to be at $\xi_{max} = 0.73\,\mu m$ with $V_{Noise} = 0.0062$. Effects of varying dose levels have been indicated and allow to estimate ξ_{max} while working under clinical dose limitations.

While it was possible to resolve the fringe of the dual-phase interferometer directly and a reliable method for signal retrieval in the single-shot mode was decided upon, it was not possible to conclusively demonstrate if the system is sensitive towards scattering caused by alveolar structures due to strong spectral and beam-hardening effects. Further investigations to deepen the understanding of the dual-phase system are required to draw such conclusions. While in theory the advantages of a dual-phase setup are a big incentive, it remains to be determined whether they carry over to eventual clinical applications.

Dark-field imaging of lungs is a powerful technique but further investigation into the underlying dynamics are required, especially when working with a dual-phase interferometer - whether it can outperform the conventional and competing methods remains to be seen.

Acknowledgement

Literature

[1] E. J. Halpern, "Triple-rule-out CT angiography for evaluation of acute chest pain and possible acute coronary syndrome", Radiology 252, 332–345 (**2009**).

[2] C. H. McCollough, S. Leng, L. Yu, and J. G. Fletcher, *Dual- and multi-energy CT: Principles, technical approaches, and clinical applications*, Sept. 2015.

[3] OECD, *Computed tomography (ct) exams (indicator)*, `https://data.oecd.org/healthcare/computed-tomography-ct-exams.htm`, (**Accessed on April 15th, 2021**).

[4] L. J. Kroft, L. Van Der Velden, I. H. Girón, J. J. Roelofs, A. De Roos, and J. Geleijns, "Added value of ultra-low-dose computed tomography, dose equivalent to chest x-ray radiography, for diagnosing chest pathology", Journal of Thoracic Imaging 34, 179–186 (**2019**).

[5] M. Fiechter et al., "Association between resting amygdalar activity and abnormal cardiac function in women and men : a retrospective cohort study", 625–632 (**2019**).

[6] Forum of International Respiratory Societies. and European Respiratory Society, *The global impact of respiratory disease* (**2017**), page 42.

[7] N. Townsend, L. Wilson, P. Bhatnagar, K. Wickramasinghe, M. Rayner, and M. Nichols, "Cardiovascular disease in Europe: epidemiological update 2016", European Heart Journal 37, 3232–3245 (**2016**).

[8] F. Pfeiffer, T. Weitkamp, O. Bunk, and C. David, "Phase retrieval and differential phase-contrast imaging with low-brilliance X-ray sources", Nature Physics 2, 258–261 (**2006**).

[9] F. Pfeiffer, M. Bech, O. Bunk, P. Kraft, E. F. Eikenberry, C. Brönnimann, C. Grünzweig, and C. David, "Hard-X-ray dark-field imaging using a grating interferometer", Nature Materials 7, 134–137 (**2008**).

[10] L. B. Gromann et al., "In-vivo X-ray Dark-Field Chest Radiography of a Pig", Scientific Reports 7 (**2017**).

[11] A. A. Fingerle et al., "Imaging features in post-mortem x-ray dark-field chest radiographs and correlation with conventional x-ray and CT", European radiology experimental 3, 25 (**2019**).

[12] K. Willer et al., "X-ray Dark-Field Chest Imaging can Detect and Quantify Emphysema in COPD Patients", medRxiv, 2021.01.15.21249798 (**2021**).

[13] F. T. Gassert et al., "X-ray Dark-Field Chest Imaging: Qualitative and Quantitative Results in Healthy Humans", Radiology, 210963 (**2021**).

[14] V. Ludwig et al., "Exploration of different x-ray Talbot-Lau setups for dark-field lung imaging examined in a porcine lung", Physics in Medicine and Biology 64, 10.1088/1361-6560/ab051c **(2019)**.

[15] K. Taphorn, F. De Marco, J. Andrejewski, T. Sellerer, F. Pfeiffer, and J. Herzen, "Grating-based spectral X-ray dark-field imaging for correlation with structural size measures", Scientific Reports 10, 13195 **(2020)**.

[16] H. Menkes and P. Macklem, "Collateral Flow", in *Handbook of physiology, the respiratory system* **(American Physiological Society, Bethesda, MD, 1986)**, pages 337–353.

[17] W. Tyler and M. Julian, "Gross and subgross anatomy of the lungs, pleura, connective tissue septa, distal airways, and structural units", in *Comparative biology of the normal lung* **(CRC Press, Boca Raton, FL, 1992)**, pages 37–48.

[18] B. M. Koeppen and B. A. Stanton, *Berne & Levy - Physiology*, edited by B. M. Koeppen and B. A. Stanton, 7th edition **(Elsevier, Philadelphia, 2018)**.

[19] C. G. Lausted, A. T. Johnson, W. H. Scott, M. M. Johnson, K. M. Coyne, and D. C. Coursey, "Maximum static inspiratory and expiratory pressures with different lung volumes", BioMedical Engineering Online 5, 29 **(2006)**.

[20] L. Ball, Y. Sutherasan, and P. Pelosi, "Monitoring respiration: What the clinician needs to know", Best Practice and Research: Clinical Anaesthesiology 27, 209–223 **(2013)**.

[21] S. D. Davis, A. S. Brody, M. J. Emond, L. C. Brumback, and M. Rosenfeld, "Endpoints for clinical trials in young children with cystic fibrosis", in Proceedings of the american thoracic society, Vol. 4, 4 **(Aug. 2007)**, pages 418–430.

[22] L. Ball, V. Vercesi, F. Costantino, K. Chandrapatham, and P. Pelosi, "Lung imaging: How to get better look inside the lung", Annals of Translational Medicine 5, 10.21037/atm.2017.07.20 **(2017)**.

[23] A. W. Reske, H. Busse, M. B. Amato, M. Jaekel, T. Kahn, P. Schwarzkopf, D. Schreiter, U. Gottschaldt, and M. Seiwerts, "Image reconstruction affects computer tomographic assessment of lung hyperinflation", Intensive Care Medicine 34, 2044–2053 **(2008)**.

[24] K. L. Boedeker, M. F. McNitt-Gray, S. R. Rogers, D. A. Truong, M. S. Brown, D. W. Gjertson, and J. G. Goldin, "Emphysema: Effect of reconstruction algorithm on CT imaging measures", Radiology 232, 295–301 **(2004)**.

[25] D. A. Lichtenstein, "Lung ultrasound in the critically ill", Annals of Intensive Care 4, 1–12 **(2014)**.

[26] G. Volpicelli et al., "International evidence-based recommendations for point-of-care lung ultrasound", in Intensive care medicine, Vol. 38, 4 **(Apr. 2012)**, pages 577–591.

[27] G. Mathis, S. Beckh, and C. Görg, "Chest Sonography", in *Chest sonography*, 4th edition **(Springer Berlin Heidelberg, Heidelberg, 2011)**, pages 51–59.

[28] F. Mojoli, B. Bouhemad, S. Mongodi, and D. Lichtenstein, "Lung ultrasound for critically ill patients", American Journal of Respiratory and Critical Care Medicine 199, 701–714 **(2019)**.

[29] P. H. Mayo, R. Copetti, D. Feller-Kopman, G. Mathis, E. Maury, S. Mongodi, F. Mojoli, G. Volpicelli, and M. Zanobetti, "Thoracic ultrasonography: a narrative review", Intensive Care Medicine 45, 1200–1211 **(2019)**.

[30] National Library of Medicine, *PubMed Query: Computed Tomography & COVID-19*, `https://pubmed.ncbi.nlm.nih.gov/?term=computed+tomography+COVID-19&filter=years.2020-2021&size=20`, **(Accessed on April 27th, 2021)**.

[31] National Library of Medicine, *PubMed Query: Ultrasound & COVID-19*, `https://pubmed.ncbi.nlm.nih.gov/?term=ultrasound+COVID-19&filter=years.2020-2021&size=20`, **(Accessed on April 27th, 2021)**.

[32] G. Volpicelli et al., "Lung ultrasound for the early diagnosis of COVID-19 pneumonia: an international multicenter study", Intensive Care Medicine 47, 444–454 **(2021)**.

[33] Y. Huang et al., "A Preliminary Study on the Ultrasonic Manifestations of Peripulmonary Lesions of Non-Critical Novel Coronavirus Pneumonia (COVID-19)", SSRN Electronic Journal, `10.2139/ssrn.3544750` **(2020)**.

[34] E. Poggiali, A. Dacrema, D. Bastoni, V. Tinelli, E. Demichele, P. M. Ramos, T. Marcianò, M. Silva, A. Vercelli, and A. Magnacavallo, "Can lung US Help critical care clinicians in the early diagnosis of novel coronavirus (COVID-19) pneumonia?", Radiology 295 **(2020)**.

[35] M. J. Fiala, "Ultrasound in COVID-19: a timeline of ultrasound findings in relation to CT", Clinical Radiology 75, 553–554 **(2020)**.

[36] A. P. Calderó, "On an inverse boundry value problem", Brazilian Mathematical Society, 65–73 **(1980)**.

[37] R. Bayford and N. Polydorides, "Focus on recent advances in electrical impedance tomography", Physiological Measurement 40, 100401 **(2019)**.

[38] A. Shono and T. Kotani, "Clinical implication of monitoring regional ventilation using electrical impedance tomography", Journal of Intensive Care 7, 4 **(2019)**.

[39] T. d. C. Martins et al., "A review of electrical impedance tomography in lung applications: Theory and algorithms for absolute images", Annual Reviews in Control 48, 442–471 **(2019)**.

[40] M. C. Bachmann, C. Morais, G. Bugedo, A. Bruhn, A. Morales, J. B. Borges, E. Costa, and J. Retamal, "Electrical impedance tomography in acute respiratory distress syndrome", Critical Care 22, 263 **(2018)**.

[41] *X-Ray Mass Attenuation Coefficients — NIST*, `https://www.nist.gov/pml/x-ray-mass-attenuation-coefficients`, (**Accessed on September 3rd, 2021**).

[42] L. Wilkinson, V. Thomas, and N. Sharma, "Microcalcification on mammography: Approaches to interpretation and biopsy", British Journal of Radiology 90 (**2017**).

[43] A. Maier, S. Seidl, V. Christlein, and J. Hornegger, *Medical Imaging Systems*, edited by A. Maier, S. Steidl, V. Christlein, and J. Hornegger, Vol. 11111, Lecture Notes in Computer Science (**Springer International Publishing, Cham, 2018**), pages 191–205.

[44] A. Yaroshenko et al., "Pulmonary Emphysema Diagnosis with a Preclinical Small-Animal X-ray DF Scatter-Contrast Scanner", Radiology 269, 427–433 (**2013**).

[45] M. Bech, A. Tapfer, A. Velroyen, A. Yaroshenko, B. Pauwels, J. Hostens, P. Bruyndonckx, A. Sasov, and F. Pfeiffer, "In-vivo dark-field and phase-contrast x-ray imaging", Scientific Reports 3, 1–3 (**2013**).

[46] A. Pandeshwar, M. Kagias, Z. Wang, and M. Stampanoni, "Modeling of beam hardening effects in a dual-phase X-ray grating interferometer for quantitative dark-field imaging", Optics Express 28, 19187 (**2020**).

[47] M. Kagias, Z. Wang, K. Jefimovs, and M. Stampanoni, "Dual phase grating interferometer for tunable dark-field sensitivity", Applied Physics Letters 110, `10.1063/1.4973520` (**2017**).

[48] J. Biederer and M. Heller, "Artificial thorax for MR imaging studies in porcine heart-lung preparations", Radiology 226, 250–255 (**2003**).

[49] J. D. Hunter, "Matplotlib: A 2D graphics environment", Computing in Science and Engineering 9, 90–95 (**2007**).

[50] E. Jones, T. Oliphant, and P. Peterson, *SciPy: Open source scientific tools for Python*, (2001) `https://www.scipy.org/`, (**Accessed on September 9th, 2021**).

[51] E. Kohda and N. Shigematsu, "Measurement of lung density by computed tomography: Implication for radiotherapy.", The Keio Journal of Medicine 38, 454–463 (**1989**).

[52] *X-Ray Mass Attenuation Coefficients — NIST*.

[53] S. M. Mostafavi, *COVID19-CT-Dataset: An Open-Access Chest CT Image Repository of 1000+ Patients with Confirmed COVID-19 Diagnosis*, (2021) `https://dataverse.harvard.edu/dataset.xhtml?persistentId=doi:10.7910/DVN/6ACUZJ`, (**Accessed on August 25th, 2021**).

[54] E. P. Judge, J. M. Hughes, J. J. Egan, M. Maguire, E. L. Molloy, and S. O'Dea, "Anatomy and bronchoscopy of the porcine lung: A model for translational respiratory medicine", American Journal of Respiratory Cell and Molecular Biology 51, 334–343 (**2014**).

[55] L. Knudsen, E. R. Weibel, H. J. G. Gundersen, F. V. Weinstein, and M. Ochs, "Assessment of air space size characteristics by intercept (chord) measurement: an accurate and efficient stereological approach", Journal of Applied Physiology 108, 412–421 **(2010)**.

[56] T. Tran, C. P. Sundaram, C. D. Bahler, J. N. Eble, D. J. Grignon, M. Francesca Monn, N. B. Simper, and L. Cheng, "Correcting the shrinkage effects of formalin fixation and tissue processing for renal tumors: Toward standardization of pathological reporting of tumor size", Journal of Cancer 6, 759–766 **(2015)**.

[57] L. H and M. W, "A species comparison of alveolar size and surface forces", Journal of applied physiology (Bethesda, Md. : 1985) 62, 1865–1871 **(1987)**.

[58] Á. Algaba and N. Nin, "Alveolar recruitment maneuvers in respiratory distress syndrome", Medicina Intensiva (English Edition) 37, 355–362 **(2013)**.

[59] S. Schleede et al., "Emphysema diagnosis using X-ray dark-field imaging at a laser-driven compact synchrotron light source", Proceedings of the National Academy of Sciences of the United States of America 109, 17880–17885 **(2012)**.

[60] K. Scherer et al., "X-ray Dark-field Radiography - In-Vivo Diagnosis of Lung Cancer in Mice", Scientific Reports 7 **(2017)**.

[61] J. Vignero, N. W. Marshall, G. V. Velde, K. Bliznakova, and H. Bosmans, "Translation from murine to human lung imaging using x-ray dark field radiography: A simulation study", PLoS ONE 13 **(2018)**.

[62] J. E. McDonough, L. Knudsen, A. C. Wright, W. Mark Elliott, M. Ochs, and J. C. Hogg, "Regional differences in alveolar density in the human lung are related to lung height", Journal of Applied Physiology 118, 1429–1434 **(2015)**.

[63] M. Strobl, "General solution for quantitative dark-field contrast imaging with grating interferometers", Scientific Reports 4, 1–6 **(2014)**.

Eigenständigkeitserklärung

Die unterzeichnete Eigenständigkeitserklärung ist Bestandteil jeder während des Studiums verfassten Semester-, Bachelor- und Master-Arbeit oder anderen Abschlussarbeit (auch der jeweils elektronischen Version).

Die Dozentinnen und Dozenten können auch für andere bei ihnen verfasste schriftliche Arbeiten eine Eigenständigkeitserklärung verlangen.

Ich bestätige, die vorliegende Arbeit selbständig und in eigenen Worten verfasst zu haben. Davon ausgenommen sind sprachliche und inhaltliche Korrekturvorschläge durch die Betreuer und Betreuerinnen der Arbeit.

Titel der Arbeit (in Druckschrift):

Why the Dark-Field Signal of Porcine Lungs can be too Bright
An Investigation of the Small-Angle-Scattering Behavior of Porcine Lungs Depending on the
Auto-Correlation Length

Verfasst von (in Druckschrift):
Bei Gruppenarbeiten sind die Namen aller
Verfasserinnen und Verfasser erforderlich.

Name(n):	**Vorname(n):**
Etter	Dominik Barnabas

Ich bestätige mit meiner Unterschrift:
 − Ich habe keine im Merkblatt „Zitier-Knigge" beschriebene Form des Plagiats begangen.
 − Ich habe alle Methoden, Daten und Arbeitsabläufe wahrheitsgetreu dokumentiert.
 − Ich habe keine Daten manipuliert.
 − Ich habe alle Personen erwähnt, welche die Arbeit wesentlich unterstützt haben.

Ich nehme zur Kenntnis, dass die Arbeit mit elektronischen Hilfsmitteln auf Plagiate überprüft werden kann.

Ort, Datum	**Unterschrift(en)**
Zürich, 13. September 2021	

Bei Gruppenarbeiten sind die Namen aller Verfasserinnen und Verfasser erforderlich. Durch die Unterschriften bürgen sie gemeinsam für den gesamten Inhalt dieser schriftlichen Arbeit.